nature communications

Article

https://doi.org/10.1038/s41467-025-66103-1

GSDME-dependent pyroptosis drives abdominal aortic aneurysm via promoting vascular senescence

Received: 20 January 2025

Accepted: 29 October 2025

Si-Jia Sun[1,2,6], Zhen Zhang[1,6], Guo-Yan Zhang[1,6], Jian-Jin Wu[3,6], Yi-Xin Zhang[1,6], Wen-Bin Wu[4], Yan Zhang[1], Hang Yin[1], Jian-Bin Zhang[1], Qi Cao[4], Jing-Wen Wu[1], Fu-Ming Shen[1], Jian Zhou[5] ✉, Dong-Jie Li[1] ✉ & Pei Wang[4] ✉

Senescence contributes to the pathology of abdominal aortic aneurysm (AAA); however, the regulation of senescence in AAA remains unclear. Here, we sought to determine the role of gasdermin-E (GSDME)-dependent non-canonical pyroptosis in AAA. GSDME-dependent non-canonical pyroptosis is activated in the lesioned vascular walls of mouse models and patients with AAA. GSDME deficiency inhibits vascular senescence and AAA progression. Combined analyses of single-cell RNA sequencing (scRNA-seq), bulk RNA-seq, and multiplex flow cytometry demonstrate that GSDME is essential for the reprogramming of vascular smooth muscle cells (VSMCs) and the shift in immune statuses of macrophages, monocytes, and neutrophils in AAA. Reintroduction of GSDME in VSMCs, but not in myeloid cells, in mice with a GSDME deletion background, recapitulates the induced vascular senescence and AAA, which is abolished by senolytic therapy with dasatinib plus quercetin. These results indicate that GSDME-dependent non-canonical pyroptosis in VSMCs may be a 'master switch' in AAA and a potential therapeutic target for managing AAA.

Senescence, characterized by the irreversible arrest of the cell cycle in response to various stresses, is emerging as a cellular hallmark of aging both in vitro and in vivo. Senescent cells actively secrete harmful substances known as the senescence-associated secretory phenotype (SASP), which can damage neighboring cells through chronic activation of the immune system and inflammation[1]. Vascular smooth muscle cells (VSMCs) critically contribute to vascular morphology, structure, and function due to their secretory plasticity. The prolonged presence of senescent VSMCs contributes to a decline in aortic function, and inadequate clearance of senescent VSMCs is closely associated with aging-related vascular diseases[1]. Conversely, protecting VSMCs from senescence is effective in slowing the development of vascular disorders[2–4].

Pyroptosis, a recently identified type of regulated cell death (RCD), was first detected in macrophages upon bacterial infection[5]. In early times, NOD-like receptor protein 3 (NLRP3) inflammasome emerged as a key mediator of pyroptosis. Until recently, it has been revealed that pyroptosis relies on the cleavage of N-terminal segments of gasdermin family members, from gasdermin A (GSDMA) to gasdermin E (GSDME), thereby causing pore formation in the cell

---

[1]Department of Pharmacy, Shanghai Tenth People's Hospital Affiliated to School of Medicine of Tongji University, Shanghai, China. [2]Department of Pharmacy, Shanghai Tenth People's Hospital Chongming Branch, School of Medicine of Tongji Unisersity, Shanghai, China. [3]Department of Vascular and Endovascular Surgery, Changzheng Hospital, Naval Medical University/Second Military Medical University, Shanghai, China. [4]The Center for Basic Research and Innovation of Medicine and Pharmacy (MOE), Department of Pharmacology, School of Pharmacy, Naval Medical University/Second Military Medical University, Shanghai, China. [5]Department of Cardiac Surgery, Shanghai Tenth People's Hospital, Tongji University School of Medicine, Shanghai, China. [6]These authors contributed equally: Si-Jia Sun, Zhen Zhang, Guo-Yan Zhang, Jian-Jin Wu, Yi-Xin Zhang. ✉e-mail: drjose@163.com; djli@tongji.edu.cn; pwang@smmu.edu.cn

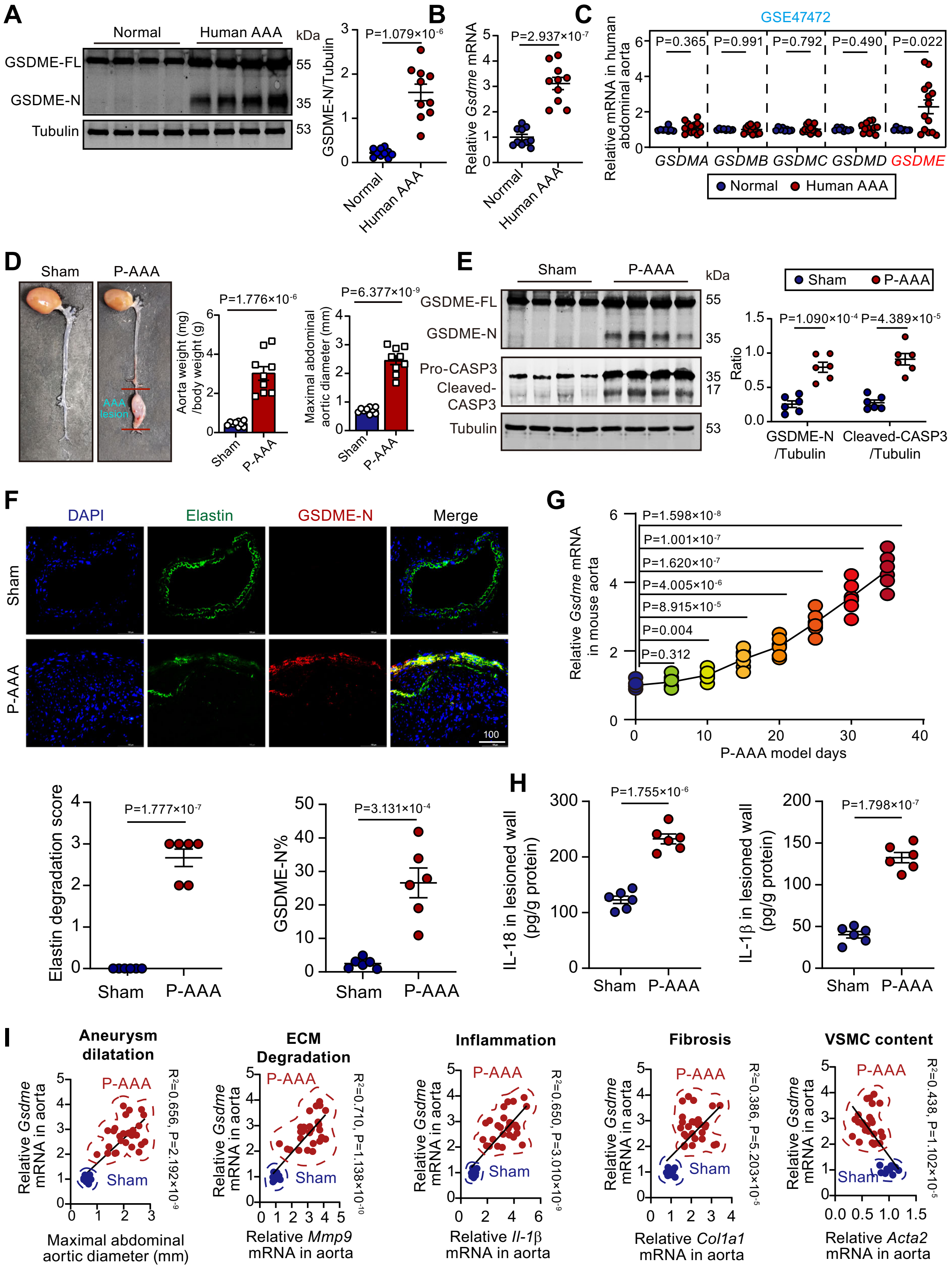

membrane and membrane rupture. During the cell lytic process, pro-inflammatory molecules like interleukin-1 (IL-1) and IL-18 are released[6]. While GSDMD is the first reported gasdermin family member mediating canonical pyroptosis after cleavage by caspase-1 or caspase-11[7,8], GSDME holds a unique position by mediating a non-canonical pyroptosis within the gasdermin family: GSDME undergoes cleavage by caspase-3, previously associated with apoptosis, a non-lytic and non-inflammatory form of RCD[9,10]. Thus, GSDME controls the balance between apoptosis and pyroptosis within normal tissue[9,10]. Our previous findings, suggest that GSDME might be involved in liver diseases[11,12]. In cardiovascular systems, recent evidence has demonstrated that GSDME promotes atherosclerosis and pulmonary arterial hypertension by inducing pyroptosis and inflammation[13,14]. Although recent results from us[15,16] and other groups[17–19] have documented the

Fig. 1 | GSDME is activated in the vascular wall of patients and mice with AAA. **A** Cleavage of GSDME was evaluated in human AAA tissues via immunoblotting analysis. Both the full-length GSDME (GSDME-FL) and the cleaved N-terminal GSDME (GSDME-N, cleaved form) were detected. Diagnosis of all AAA patients relied on clinical examination, including contrast-enhanced MRI. Lesion AAA tissue was obtained during aneurysm resection. *N* = 10 biological replicates. **B** The transcriptional level of GSDME in AAA tissues was assessed using qPCR analysis. *N* = 10 biological replicates. **C** Comparison of mRNA expression levels of five gasdermin family members (GSDMA, GSDMB, GSDMC, GSDMD, and GSDME) between the vasculatures of patients with AAA (*N* = 14) and control aortic specimens from organ donors (*N* = 8) was conducted using a public Gene Expression Dataset (GEO accession number GSE47472). **D** Morphological changes in the mouse aorta tree with P-AAA were observed. P-AAA was induced by porcine pancreatic elastase (PPE) surgery along with β-aminopropionitrile (BAPN) intake via water. Aorta weight and maximal abdominal aortic diameter in Sham-operated mice and P-AAA mice were calculated. *N* = 9 biological replicates. P-AAA, PPE + BAPN-induced AAA. **E** Immunoblotting analyses were performed to assess the cleavage of GSDME and its upstream caspase-3 (CASP3) in lesion tissues of P-AAA mice. *N* = 6 biological replicates. **F** Double-immunofluorescent staining revealed the degradation of elastin and induction of GSDME-NT in AAA lesion tissue of mice. *N* = 6 biological replicates. **G** Changes in Gsdme mRNA levels during the entire course of AAA were examined. *N* = 6 biological replicates. **H** The protein levels of interleukin-18 (Il-18) and Il-1β, two downstream pro-inflammatory factors of GSDME-dependent pyroptosis, were quantified by ELISA in AAA lesion tissue. *N* = 6 biological replicates. **I** The association between Gsdme mRNA levels and aneurysm dilatation (abdominal aortic diameter), extracellular matrix degradation (*Mmp9* mRNA expression), inflammation (*Il-1β* mRNA expression), fibrosis (*Col1α1* mRNA expression), and VSMC content (*Acta2* mRNA expression) was investigated. Data were presented as mean ± SEM. Unpaired Student's *t*-tests (**A**–**H**) or linear regression (**I**) were performed. P-AAA, PPE + BAPN-induced AAA.

detrimental role of pyroptosis in AAA, the intricate importance and regulatory patterns of GSDME in AAA, are still largely unknown.

Abdominal aortic aneurysms (AAAs) are severe CVDs characterized by progressive dilation of the aorta. Rupture following AAA is lethal, with mortality rates about 90%[20]. AAA is accompanied by chronic inflammation within the vasculature, VSMC remodeling and death, and extravascular matrix degradation[20]. Currently, surgical repair is still the only available therapeutic approach for patients with AAA. Although many endeavors have been carried out to assess the efficacy of antihypertensive agents, statins, doxycycline, or antiplatelet drugs, none of them has convincingly limited AAA[21]. Thus, a deeper understanding of AAA pathogenesis at the molecular level is necessary to explore potential medications for AAA patients.

In this study, we reveal that GSDME-dependent non-canonical pyroptosis is activated in the vasculature of patients and mouse models with AAA. Deletion of GSDME inhibits the SASP secretome and immune cell infiltration in AAA vasculature. Using combined bulk RNA-sequencing (RNA-seq) and single-cell RNA-sequencing (scRNA-seq) analyses, we demonstrate that GSDME is a critical driver of senescent phenotype in VSMCs and immune cells in AAA lesion vasculature.

Results

GSDME-dependent non-canonical pyroptosis is activated in AAA

To assess changes in GSDME expression in human AAA lesions, we compared normal aortic tissue with AAA tissue ($n = 10$ biological replicates, clinical information in Supplementary Table 1). While full-length GSDME (GSDME-FL) moderately increased in human AAA tissue, the cleaved N-terminal fragment (GSDME-N) was exclusively detected in AAA tissue, not in controls (Fig. 1A). Similar changes were observed in *GSDME* mRNA expression (Fig. 1B). In a gene expression profile of biopsies from human AAA tissue (No. GSE47472), only *GSDME* transcriptional level increased, while other gasdermin family members (*GSDMA, GSDMB, GSDMC* and *GSDMD*) remained unchanged (Fig. 1C). Accordingly, *Caspase-3* was the most abundant caspase in AAA lesions (Fig. S1A). Notably, *CASPASE-3*, but not *CASPASE-1* or *CASPASE-4/5*, was significantly upregulated in AAA lesion tissues compared to normal arteries (Fig. S1B).

To validate these findings, we developed a murine AAA model (termed P-AAA) by infusing porcine pancreatic elastase (PPE) into the abdominal aorta alongside continuous administration of β-aminopropionitrile monofumarate (BAPN), a lysyl-oxidase inhibitor that enhances elastin degradation[22]. AAA pathologies were confirmed through morphological changes, increased whole aorta weight, and abdominal aortic dilation (Fig. 1D). Significant cleavage of GSDME and caspase-3 was detected in AAA lesions (Fig. 1E), further validated by immunohistochemistry (Fig. 1F). During AAA progression, *Gsdme* mRNA expression increased progressively (Fig. 1G). Pro-inflammatory factors IL-1β and IL-18, released via GSDME-dependent pyroptosis, were upregulated in AAA lesions (Fig. 1H). Notably, *Gsdme* expression correlated positively with maximal aortic diameter, *Mmp9* (extracellular matrix degradation), *Il-1β* (inflammation), and *Col1a1* (fibrosis), while inversely correlating with *Acta2* (SMC marker) (Fig. 1I). Caspase-3, but not Caspase-1 or Caspase-6, was specifically significantly upregulated in AAA lesion tissue from the mouse model (Fig. S1C–E). To further investigate the potential role of the GSDME–caspase-3 axis in AAA, we established another AAA mouse model (A-AAA) by infusing angiotensin II (Ang II) via osmotic pump into ApoE$^{-/-}$ mice[23,24]. Caspase-3, but not caspase-1 or caspase-6, was significantly upregulated in AAA tissues of this model (Fig. S1F–G), suggesting possible activation of GSDME-dependent cell death rather than canonical pyroptosis. Analysis of a public scRNA-seq dataset of mouse AAA tissues (GSE239620) revealed that GSDMD was predominantly expressed in immune cells—particularly monocytes and macrophages—whereas GSDME was abundantly expressed in VSMCs and significantly upregulated in AAA (Fig. S2A, B). Flow cytometry confirmed that GSDME, rather than GSDMD, was markedly upregulated in α-SMA$^+$ VSMCs (Fig. S2C, D). Although VSMCs produced small amounts of IL-18 and IL-1β, these cytokines were mainly secreted by immune cells (Fig. S2E, F), implying that GSDME-mediated VSMC pyroptosis may contribute to AAA pathogenesis through mechanisms beyond direct cytokine release. Collectively, these findings support a potential role for GSDME-dependent pyroptosis in AAA.

Global knockout of GSDME alleviates AAA pathologies

Based on our observations that GSDME is expressed in VSMCs and upregulated in AAA lesions, we next investigated whether GSDME contributes causally to AAA pathogenesis in vivo. We induced the P-AAA model in both male GSDME global knockout (KO) and wild-type (WT) mice. In this model, KO mice exhibited a higher survival rate than their WT counterparts (Fig. 2A), and postmortem examination confirmed that death was attributable to aortic rupture secondary to AAA (Fig. S3A). Ultrasound analysis revealed that GSDME deletion attenuated the progressive enlargement of the maximal aortic diameter (Fig. 2B). Consistently, KO mice had significantly lower aortic weight compared with WT mice (Fig. 2C). Notably, this protective effect of GSDME deficiency against AAA was also observed in female mice (Fig. S3B). Haematoxylin and eosin (H&E) and elastin-Van Gieson (EVG) staining revealed that KO mice exhibited attenuated medial structural disruption (Fig. 2D) and preserved elastin integrity (Fig. 2E). Immunofluorescence analysis further showed that GSDME deletion decreased matrix metalloproteinase-9 (MMP9) expression without affecting tissue inhibitor of metalloproteinases-1 (TIMP1) levels (Fig. 2F). Flow cytometry using the SYTOX fluorescence probe, which labels dying cells, on single-cell suspensions from AAA lesion walls demonstrated that cell death occurred predominantly in VSMCs rather than immune cells, and was significantly reduced in VSMCs of KO mice (Fig. 2G), consistent with reduced pyroptotic and other lytic cell death in VSMCs.

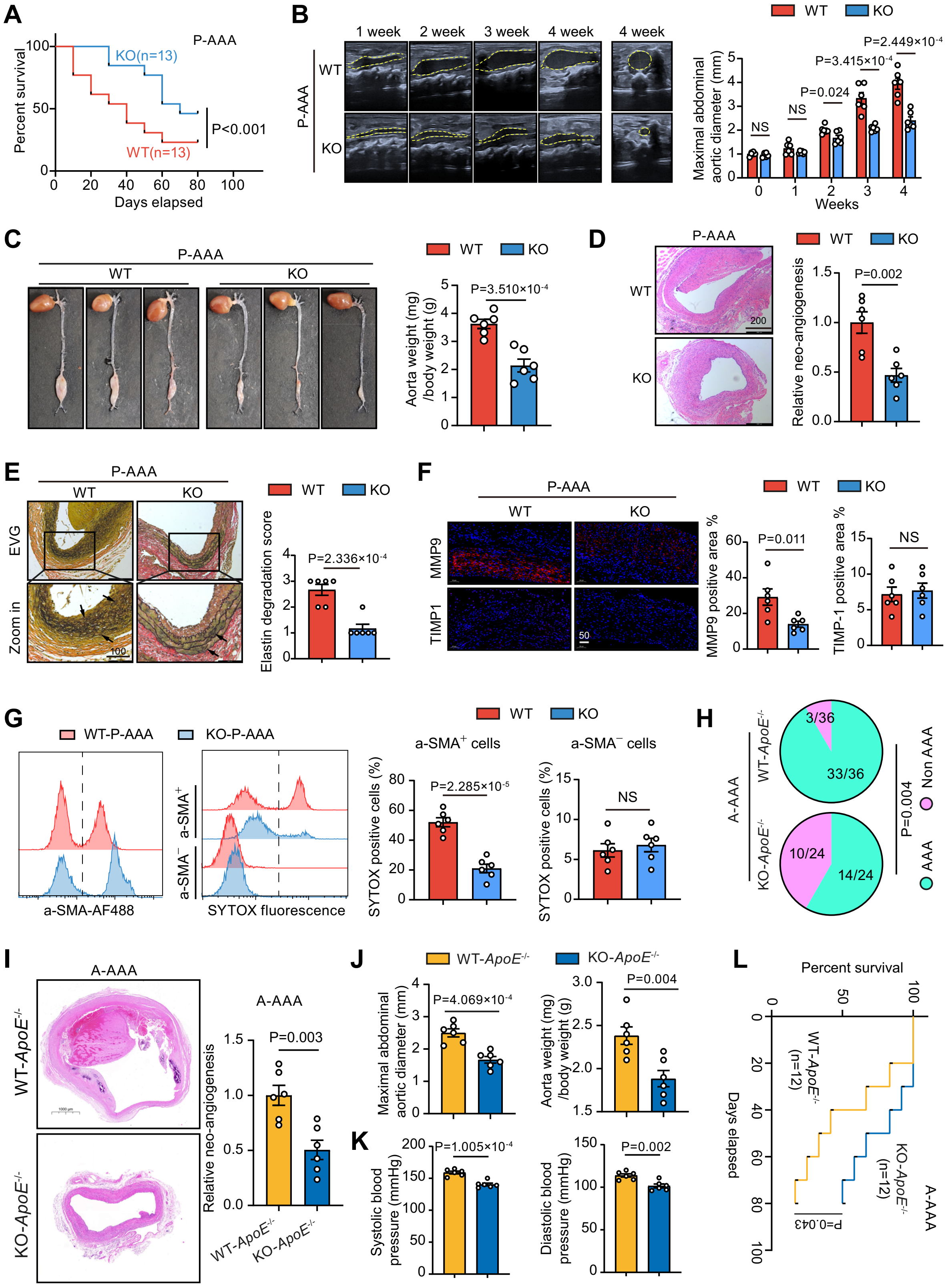

To determine whether this protective effect also applies to a hyperlipidemia-associated AAA setting, we further evaluated the role of GSDME in AAA using the A-AAA model. GSDME knockout (KO) mice were crossed with ApoE$^{-/-}$ mice to generate KO-ApoE$^{-/-}$ mice, which, along with WT-ApoE$^{-/-}$ controls, were infused with a high dose of angiotensin II via osmotic pump for 4 weeks. In this model, KO-ApoE$^{-/-}$ mice exhibited a lower AAA incidence than WT-ApoE$^{-/-}$ mice (Fig. 2H). H&E staining revealed that KO-ApoE$^{-/-}$ mice exhibited attenuated medial structural disruption (Fig. 2I). They also showed reduced aortic weight and abdominal aortic diameter (Fig. 2J), as well as attenuated increases in both systolic and diastolic blood pressure (Fig. 2K). Although reduced blood pressure may partially contribute to the phenotype, the magnitude of AAA suppression suggests additional vascular wall-specific protective mechanisms. Consistent with these

Fig. 2 | Global knockout of GSDME alleviates AAA pathologies in mouse models. **A** Survival curve of wild-type (WT) and *Gsdme* knockout (KO) mice after P-AAA formation. **B** Representative images and quantification of the maximal diameter of the abdominal aorta visualized by ultrasound in WT and KO mice with the P-AAA model. **C** Representative morphology and quantitative analysis of aortic weight in WT and KO mice with the P-AAA model. **D** Representative H&E staining in P-AAA vasculature of WT and KO mice. **E** Representative elastin-Van-Gieson (EVG) staining and elastin degradation score in P-AAA vasculature of WT and KO mice. **F** Representative immunofluorescence staining and quantitative analysis of MMP9 and TIMP1 in lesion vasculature of WT and KO mice with the P-AAA model. **G** Flow cytometry analysis of dying cells (SYTOX dye-positive) in a-SMA$^+$ cells or a-SMA$^-$ cells from P-AAA vasculature of WT and KO mice. **H** Incidence rate of A-AAA in angiotensin II (Ang II)-infused WT-ApoE$^{-/-}$ mice and KO-ApoE$^{-/-}$ mice. A-AAA refers to Ang II-induced AAA. The reported numbers (36 WT-ApoE$^{-/-}$ and 24 KO-ApoE$^{-/-}$) represent the cumulative use across multiple experimental procedures (molecular assays, flow cytometry, histopathology, and survival analyses). **I** Representative H&E staining in A-AAA vasculature of WT-ApoE$^{-/-}$ mice and KO-ApoE$^{-/-}$ mice. **J** Analysis of aortic weight and maximal abdominal aortic diameter in WT-ApoE$^{-/-}$ mice and KO-ApoE$^{-/-}$ mice with A-AAA. **K** Systolic and diastolic blood pressure in WT-ApoE$^{-/-}$ mice and KO-ApoE$^{-/-}$ mice with A-AAA. **L** Survival curve of WT-ApoE$^{-/-}$ mice and KO-ApoE$^{-/-}$ mice after A-AAA formation. Data are presented as mean ± SEM. $N = 6$ biological replicates unless otherwise indicated. The Chi-squared test was performed in (**H**), the Log-Rank test was performed in (**A**) and (**L**), and unpaired Student's *t*-tests were performed in the remaining panels. P-AAA refers to PPE + BAPN-induced AAA, and A-AAA refers to Ang II-induced AAA.

protective effects, KO-ApoE$^{-/-}$ mice displayed improved survival compared with WT-ApoE$^{-/-}$ mice (Fig. 2L). Collectively, these results indicate that global GSDME deficiency mitigates AAA progression across distinct experimental models.

GSDME controls the infiltration and inflammatory status of Mφ/Mo in AAA

The prominent immune cell infiltration, especially myeloid cells composed of Mφ/Mo and neutrophils, in the damaged aortic wall and subsequent phenotypic modulation based on microenvironmental cues play key roles in the progression of AAA[20]. Next, we investigated the potential influence of GSDME deletion on vascular myeloid cell populations. CD45$^+$ single leukocytes were isolated from AAA lesion tissue of WT and KO mice using magnetic-activated cell sorting and analyzed with multiplex flow cytometry. Antibodies against CD11b, Ly6G, F4/80, TIM4, MHCII, and Ly6C were used for staining, and an unbiased nonlinear high-dimensional analysis was employed (Fig. 3A). Among these markers, TIM4 emerges as a well-established marker of inflammation-resolving tissue-resident Mφ (TRM) across organs[25], while MHCII is a signature of activated Mφ with antigen-presentation activity[26]. Using t-distributed stochastic neighbor embedding (t-SNE)-guided gating, several myeloid cell clusters, including Ly6C^{hi} Mo, Ly6C^{Int} Mo, Ly6C^{lo} Mo, MHCII$^+$ Mφ, TIM4$^+$ Mφ, MHCII$^-$TIM4$^-$ Mφ (double-negative Mφ, DN Mφ), and Ly6G$^+$ neutrophils, were identified (Fig. 3B). Differences in the distributions of Mφ/Mo and neutrophils were observed between the AAA lesion tissue from WT and KO mice (Fig. 3C). In the heatmap, decreased frequencies of Ly6C^{hi} Mo and MHCII$^+$ Mφ, as well as increased distribution of Ly6C^{lo} Mo and TIM4$^+$ Mφ, were significantly noted in AAA tissue of KO mice compared with WT mice (Fig. 3D).

The impact of GSDME on Mφ/Mo populations was further assessed using flow cytometry with manual gating (gating strategy in Fig. S4). The AAA tissue of KO mice showed reduced frequencies of Mφ and Mo compared to that of WT mice (Fig. 3E). The number of inflammation-resolving TIM4$^+$ Mφ in AAA tissue of KO mice was significantly higher than that of WT mice, while the number of MHCII$^+$ Mφ in AAA tissue of KO mice was lower than that of WT mice (Fig. 3F). The number of Ly6C^{hi} Mo, which are classical pro-inflammatory Mo, was lower in AAA tissue of KO mice, while the number of inflammation-resolving Ly6C^{lo} Mo was higher in AAA tissue of KO mice (Fig. 3G). Consistent with the flow cytometry findings, immunofluorescence analysis further confirmed that GSDME knockout markedly reduced macrophage infiltration in AAA lesions (Fig. 3H). These results emphasize that GSDME regulates the infiltration and inflammatory status of Mφ/Mo in the vascular wall of AAA.

Global knockout of GSDME inhibits VSMCs' senescence in AAA

Recently, we discovered that cell death activation triggers vascular senescence and dysfunction[27]. Thus, we next investigated GSDME's role in AAA-related senescence regulation. Senescence-associated β-galactosidase (SA-β-gal) staining revealed massive senescent cells in the AAA lesion vasculature of WT mice compared to KO mice (Fig. 4A). Senescence molecular markers such as p21[28], p53, p16[29], and phospho-H2A.X^{Ser139} (γH2A.X)[30] were significantly upregulated in WT-AAA mice but less pronounced in KO-AAA mice (Fig. 4B). Flow cytometry analysis revealed that GSDME knockout preferentially alleviated senescence in VSMCs, with no significant effect on immune cells or endothelial cells (Fig. 4C, Fig. S5A–C). Immunofluorescence staining for p16 revealed higher expression in WT-AAA mice compared to KO-AAA mice, particularly in the vascular tunica media (Fig. 4D). Analysis of the SASP secretome revealed significantly lower mRNA levels of pro-inflammatory factors (Fig. S5D) and chemokines (Fig. S5E) in lesion vasculature of KO-AAA mice compared to WT-AAA mice. Consistently, SASP-related damage-associated molecular patterns (DAMPs) like *Icam1, Vcam1, Gdf15*, and *Igfbp2* exhibited consistent changes in both WT and KO-AAA mice (Fig. S5F). Moreover, mRNA levels of matrix metalloproteinases (*Mmp2* and *Mmp9)*, as well as protein levels of high mobility group box-1 (HMGB1), were induced in WT-AAA mice to a lesser extent in KO-AAA mice (Fig. S5G, H). The mRNA levels of iNOS and H2-DMa showed similar results (Fig. S5I, J).

In vitro studies using primary mouse VSMCs treated with Ang II demonstrated GSDME cleavage at 3 h post-treatment (Fig. 4E). Notably, GSDME cleavage was more pronounced when cells were treated with Ang II plus bleomycin (BLM), an agent with potent DNA-attacking activity for inducing vascular senescence[27,31] (Fig. 4E). Il-1β was released in the Ang II + BLM-treated VSMCs in a time-dependent manner (Fig. 4F). Senescence induction, as indicated by SA-β-gal staining, was observed in Ang II + BLM-treated VSMCs at day 2 post-treatment (Fig. 4G). Treatment with Ang II + BLM also induced the expression of senescence-related molecules (p53, p16, and p21) in human VSMCs, but not in myeloid cells, suggesting a VSMC-specific senescence response (Fig. S5K, L). As GSDME's cleavage seems to occur earlier than senescence induction, we compared senescence between VSMCs isolated from WT and KO mice to ascertain GSDME's essential role in vascular senescence. Comparative analysis revealed attenuated proportion of SA-β-gal-positive senescent cells (Fig. 4H), accompanied by decreased proportion of p16$^+$ senescent cells and p21$^+$ senescent cells (Fig. 4I), expression of senescence markers (Fig. 4J) and SASP factors (Fig. 4K) in GSDME knockout VSMCs. These findings underscore the essential role of GSDME in AAA-associated vascular senescence.

Combined bulk RNA-seq and scRNA-seq transcriptional profiling reveals that GSDME deficiency alleviates senescence in AAA

Lesion AAA tissues from WT and KO mice were subjected to combined RNA-seq and scRNA-seq (Fig. 5A). Compared to WT-AAA tissue, KO-AAA tissue exhibited differential gene expression, with 78 upregulated and 309 downregulated genes (fold change >2 or <0.5, $p < 0.05$, Fig. 5B and Supplementary Data 1). Integrative functional analysis revealed enhanced extracellular matrix organization but reduced immune system activity and p53 pathway in KO-AAA tissue (Fig. 5C). Additionally, a chord plot indicated decreased neutrophil aggregation, cell adhesion, inflammation, and secretory vesicle activity (Fig. 5D). Several well-known

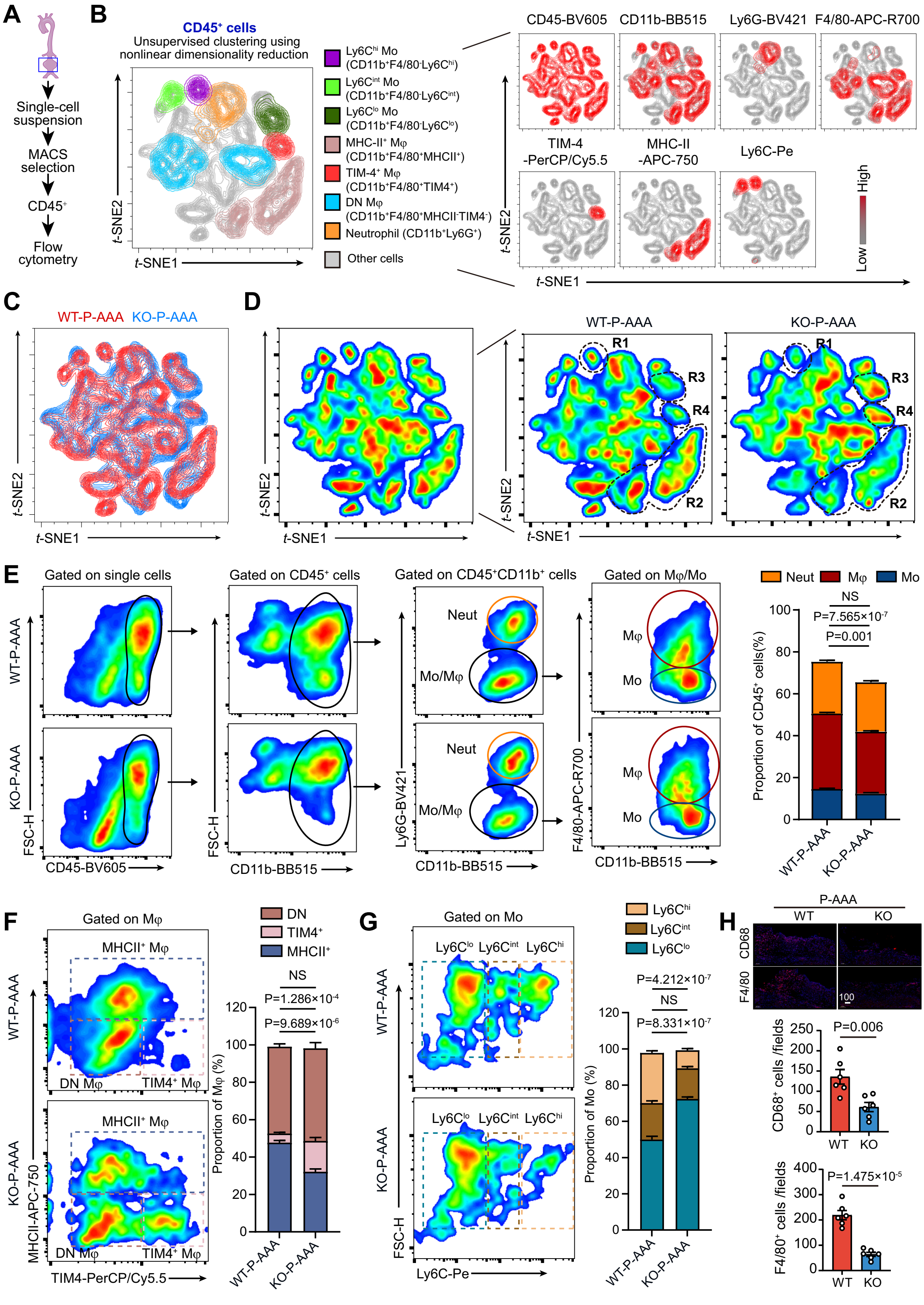

senescence-associated molecules, including *Cxcl5* (ligand of Cxcr2)[32], *Mmp12, Il6, Il1α*, and *S100* family, were highlighted in the chord plot (Fig. 5D). KEGG analysis showed that the processes of immune system, cell senescence and cell adhesion molecules were inhibited, while *Mmp12, Il6, Il1a, Cxcl5*, and *Cxcr2* were enriched in the cell senescence process (Fig. 5E). These findings suggest that GSDME deletion inhibits immune/inflammation and senescence processes.

In scRNA-seq analysis, transcriptomes from 14,393 single intravascular cells were obtained from WT-AAA and KO-AAA tissues post-quality control and filtering. Major cell types, including VSMCs (*Ccn1*⁺), Mφ (*Cd68*⁺), Mo (*Ly6C*⁺), endothelial cells (*Pecam1*⁺), granulocyte (*Ly6G*⁺), B cells (*Cd79a*⁺), dendritic cells (*Cd209a*⁺), and T cells (*Cd3e*⁺), were identified (Fig. 5F, G). Compared to WT-AAA tissue, KO-AAA tissue showed increased proportions of SMCs and reduced proportions

Fig. 3 | Multiplexed flow cytometry reveals the regulatory action of GSDME on infiltration and status of macrophages/monocytes in the vascular wall of AAA. **A** Representative experimental design of multiplexed flow cytometry in CD45$^+$ immune cells isolated from AAA lesion vasculature. **B** High-dimensional analysis of multiplexed flow cytometry using an unbiased nonlinear dimensionality reduction algorithm (t-distributed stochastic neighbor embedding, t-SNE) to identify clustering of subpopulations in CD45+ cells isolated from AAA lesion vasculature. Live CD45$^+$ leukocyte cells were gated with macrophages/monocytes-related markers (CD11b, Ly6G, F4/80, TIM4, MHCII, and Ly6C). The multiplexed flow cytometry results were concatenated, transformed, and plotted in 2D t-SNE plots using R software. The subgroups of macrophages/monocytes are indicated in the image. **C** Comparison of t-SNE dimensionality reduction and embedding of CD45$^+$ cells pooled from vasculatures of WT (red) and KO (blue) mice with AAA. **D** Heatmap showing the differences in t-SNE dimensionality reduction and embedding of CD45$^+$ cells from vasculatures of WT and KO mice with AAA. Four different regions (R1 to R4) are indicated by dotted lines. Their properties are indicated in (**B**). **E** Representative flow cytometry plots and quantification analyses with manual gating on the proportions of neutrophils, macrophages, and monocytes within CD45$^+$ cells from vasculatures of WT and KO mice with AAA. **F** Representative flow cytometry plots and quantification analyses on the subclusters of macrophages by markers of TIM4 and MHCII. The TIM4$^+$ macrophages, MHCII$^+$ macrophages, and double-negative macrophages (DN-macrophages) were gated and calculated. **G** Representative flow cytometry plots and quantification analyses on the subclusters of monocytes by markers of Ly6C. The Ly6C^{hi} monocytes, Ly6C^{int} monocytes, and Ly6C^{lo} monocytes were gated and calculated. **H** Representative immunofluorescence staining and quantitative analysis of CD68 and F4/80 in lesion vasculature of WT and KO mice with the P-AAA model. Data are presented as mean ± SEM. $N = 6$ biological replicates. Unpaired Student's *t*-tests were used. P-AAA refers to PPE + BAPN-induced AAA.

---

of myeloid cells (Mφ, Mo, and neutrophils) (Fig. 5H). Gene set variation analysis (GSVA) revealed significant pathway alterations in VSMCs and myeloid cells: in VSMCs and myeloid cells, immune/inflammation-related pathways, including the toll-like receptor pathway, JAK-STAT signaling pathway, MAPK signaling pathway, etc., as well as the senescence-related pathways such as chemokine signaling and p53 signaling, were inhibited, while oxidative phosphorylation and muscle contraction were enhanced (Fig. 5I).

Cell-cell communication network was generated using the scRNA-seq analysis package CellChat. It highlighted VSMCs and myeloid cells as major contributors to intercellular interactions in AAA lesion vasculature (Fig. 5J). In the AAA lesion vasculature of KO mice, communication between VSMCs and Mo or Mφ increased, while communication between Mo and Mφ, and Mφ and neutrophils, decreased (Fig. 5K). Numerous secreting and targeting cells, including well-established SASP secretome factors, were identified, with VSMCs appearing as major targets (Fig. 5L). These SASP secretome factors included *Tnf, secreted phosphoprotein 1 (Spp1), visfatin, Il-6*, etc. On the contrary, the fibroblast growth factor (FGF) pathway with potent anti-senescent activity[33], was induced. Further analysis revealed reduced outgoing signals in VSMCs, Mφ, and neutrophils, but not Mo, and reduced incoming signals in Mφ and neutrophils, but not VSMCs and Mo, in AAA tissue of KO MICE (Fig. S6A, B). These findings elucidate that GSDME knockout suppresses the senescence-associated transcriptional signature and cell status in AAA lesion vasculature.

GSDME facilitates reprogramming of VSMCs into a pro-senescent phenotype in AAA

In pathological aortic aneurysms, VSMCs exhibit a high degree of plasticity, transitioning from a contractile state to several intermediate cell types, including macrophage-like, osteogenic-like, mesenchymal-like, fibroblast-like, and adipose-like phenotypes[34]. A total of five VSMC subgroups were identified using unbiased UMAP clustering (Fig. 6A–C): contractile VSMCs (VSMCs-1, *Myh11*$^+$*Acta2*$^+$*Tagln*$^+$*Actn1*$^+$), mesenchymal-like VSMCs (VSMCs-2, *Fstl1*$^+$*Sca1*$^+$*Pi16*$^+$*Timp1*$^+$), osteogenic-like VSMCs (VSMCs-3, *Sox5*$^+$*Flnb*$^+$*Bmper*$^+$*Meg3*$^+$), Mφ–like VSMCs (VSMCs-4, *Lyz2*$^+$*Cd84*$^+$*Laptm5*$^+$*Il1b*$^+$), and fibroblast–like VSMCs (VSMCs-5, *Gsn*$^+$*Ogn*$^+$*Gdf10*$^+$*Col6a5*$^+$). Functional analysis revealed activated signaling pathways or biological processes in each VSMC subgroup, notably cytokine production and cell senescence enrichment in macrophage-like VSMCs (Fig. 6D). While the proportion of contractile VSMCs (VSMCs-1) was relatively low in AAA tissues of both WT and KO mice, more contractile VSMCs were retained in AAA tissues of KO mice (Fig. 6E). In KO-AAA tissue, the proportions of macrophage-like and fibroblast-like VSMCs decreased, while the proportions of mesenchymal-like and osteogenic-like VSMCs increased (Fig. 6E). Pseudotime trajectory analysis revealed dynamic differentiation of VSMC subtypes during AAA (Fig. 6F). Contractile VSMCs (VSMCs-1) were identified as original-state VSMCs, branching into two different trajectories, forming macrophage-like VSMCs (VSMCs-4) and mesenchymal-/fibroblast-like VSMCs (VSMCs-2/5) (Fig. 6F). Compared to AAA tissues of WT mice, AAA tissues of KO mice exhibited enhanced extracellular matrix and elastic fiber formation, along with reduced signaling pathways in interleukins, collagen formation, IL-18, IL-1, and programmed cell death (Fig. 6G). These findings suggest that GSDME deletion inhibits the progression toward a pro-senescent status of VSMCs in the AAA lesion.

GSDME contributes to the switch of the immune and inflammation status of myeloid cell subsets in AAA

Next, we investigated the impact of GSDME deletion on subsets of myeloid cells (Mφ/Mo and neutrophils) in AAA lesions. Mφ/Mo were further classified into four subgroups each (Mo1-4 and Mφ1-4, Fig. S7A). As illustrated in Fig. S7B, Mo1 appeared to be non-classical monocytes *(Ace*$^+$*Treml4*$^+$*Il1r2*$^+$*)*[35], while Mo2 exhibited characteristics of classical monocytes with early leukocyte markers (*Sell*$^+$*Cd177*$^+$*Nrg1*$^+$). Mo3 were identified as infiltrating monocytes (*Ccr2*$^+$*Ciita*$^+$*Clec4b1*$^+$), and Mo4 represented a group of dendritic cell-like monocytes (*CD226*$^+$*Aldh1a2*$^+$*Klrk1*$^+$). Mφ1 displayed features of immunostimulatory macrophages (*Tnf*$^+$*Nlrp3*$^+$*Cxcl16*$^+$), whereas Mφ2 exhibited characteristics of immunosuppressive tissue-repairing macrophages (*Arg1*$^+$*Spp1*$^+$*Cav1*$^+$). Mφ3 were identified as TRM (*Lyve1*$^+$*Fcna*$^+$*Folr2*$^+$)[25], while Mφ4 represented a highly polarized IFN-responsive subgroup (*Ifit1*$^+$*Ifit2*$^+$*Ifit3*$^+$). Among monocytes, Mo2 and Mo3 showed increased activities in cytokine and chemokine production, while Mo4 displayed higher antigen processing/presentation activity (Fig. S7C). Among macrophages, Mφ1 demonstrated high activities in acute/chronic inflammatory response, while Mφ2 and Mφ3 exhibited potent activities in phagocytosis, apoptotic cell clearance, and tissue remodeling. Mφ4 exhibited the strongest response to cytokine and interferon (Fig. S7C). Radar plot analysis revealed distinct contributions of Mo1-4 and Mφ1-4 to various cellular functions (Fig. S7D). Pseudotime trajectory analysis indicated that Mo2, as primary-state monocytes, branched into two trajectories, leading to the formation of Mφ1 and Mφ3/Mφ4 (Fig. S7E). The AAA tissue from KO mice showed a decreased proportion of Mφ1 and an increased proportion of Mφ3/Mo4 compared to WT-AAA tissue (Fig. S7F), suggesting that GSDME deletion inhibits the reprogramming of Mφ/Mo subsets toward the pro-inflammatory status.

Neutrophils within the vasculature of AAA lesions were further classified into four groups: Neutrophils-1 (*Tnf*$^+$*Dusp2*$^+$*Nr4a1*$^+$*Icam1*$^+$), Neutrophils-2 (*Cstb*$^+$*Bnip3*$^+$*Sqstm1*$^+$*Egr1*$^+$), Neutrophils-3 (*Syne1*$^+$*Arhgap15*$^+$*Adgre1*$^+$*Lrrk2*$^+$,) and Neutrophils-4 (*Cxcr2*$^+$*Mmp8*$^+$*Tlr2*$^+$*Arg2*$^+$, Fig. S8A–C). In KO mice, the proportion of Neutrophils-1 and 2 was enhanced, while the proportions of Neutrophils-4 were reduced (Fig. S8D). Pseudotime trajectory analysis revealed dynamic differentiation of neutrophil subtypes during AAA: Neutrophils-1 were identified as original-state neutrophils, branching into two different trajectories, forming Neutrophils-3 and Neutrophils-4,

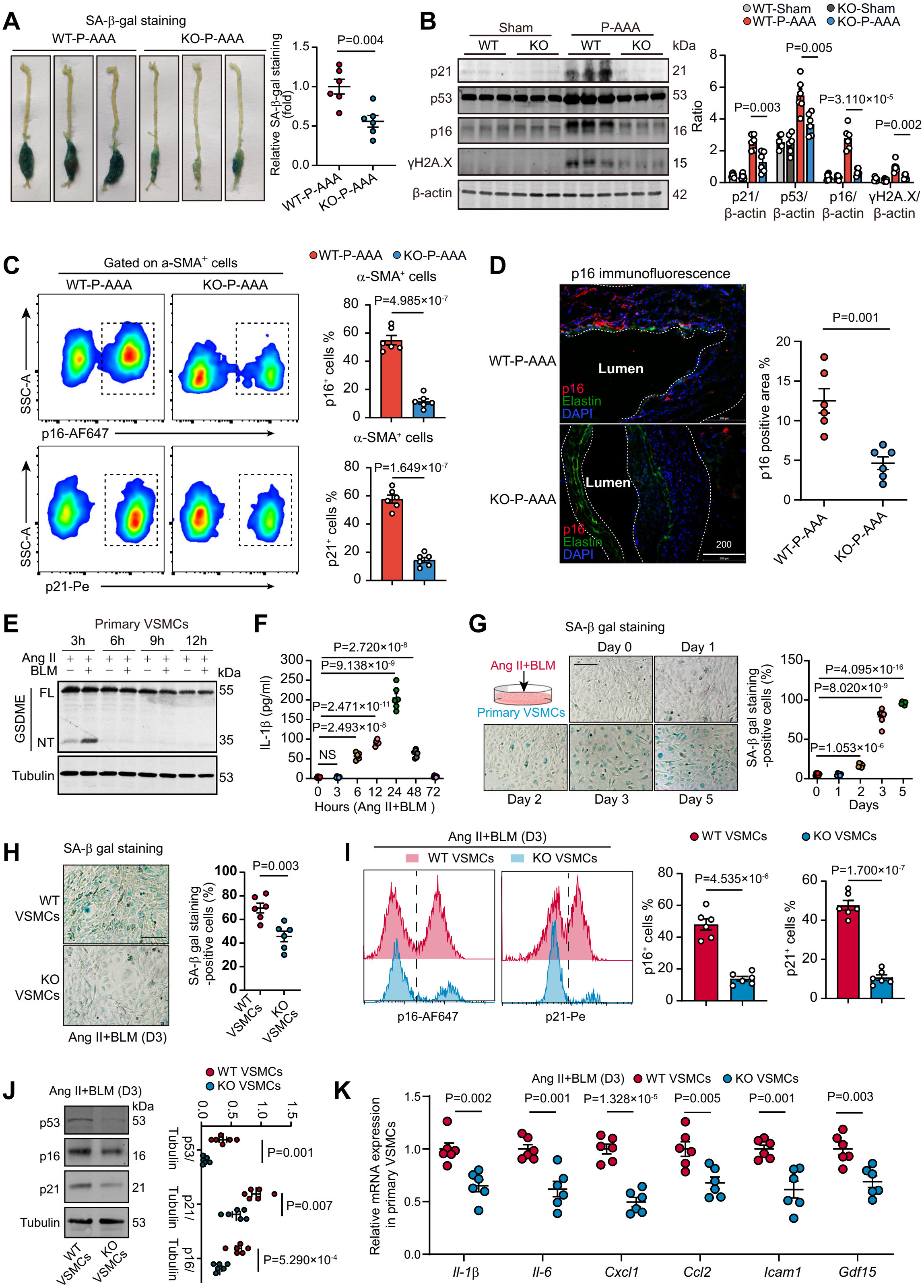

while Neutrophils-2 were intermittent-state neutrophils (Fig. S8E). Neutrophils-4 appeared to be a group of senescent neutrophils due to their high expression of *Cxcr2*, a well-established chemokine that induces neutrophil senescence[32]. Neutrophils-3 resembled macrophages due to their high expression of *Adgre1* (also known as F4/80) and *Lrrk2*, two important molecules for macrophage phagocytosis. *Cxcr2*, together with its ligand *Cxcl2*, demonstrated the lowest expression in neutrophils-1 but the highest expression in neutrophils-4 (Fig. S8F). Since KO mice had a lower proportion of late-stage senescent neutrophils (Neutrophils-4), these results suggest that *Gsdme* deletion blunted the toward of neutrophils to a senescence state.

Fig. 4 | GSDME is essential for the vascular senescence during AAA. **A** Representative morphology of aorta trees with P-AAA stained by SA−β-gal staining. Aortae were isolated from WT and KO mice with P-AAA. Tissues with senescence display blue-staining after SA−β-gal staining. **B** Protein expressions of senescence markers (p21, p53, p16, and γH2A.X) in P-AAA tissue of WT and KO mice were evaluated by immunoblotting. **C** Flow cytometry of p16-positive senescent cells and p21-positive senescent cells in a-SMA$^+$ cells from AAA lesion vasculatures of WT and KO mice. **D** Representative immunofluorescent staining of senescence marker p16 in P-AAA lesion from WT and KO mice. Elastin was stained for visualization of the vascular wall. Nuclei were stained by DAPI. **E** Cleavage of GSDME protein in cultured mouse VSMCs treated by Ang II alone or Ang II + BLM (bleomycin). **F** IL-1β concentration in the culture medium of mouse VSMCs treated by Ang II + BLM at different timepoints. **G** Representative SA-β-gal staining and quantitative analysis of mouse VSMCs treated by Ang II + BLM at different timepoints. **H** Representative SA-β-gal staining and quantitative analysis of VSMCs isolated from WT or KO mice treated by Ang II + BLM for 3 days. **I** Flow cytometry analysis of the senescent cells (p16-positive, p21-positive) in WT and KO VSMCs treated by Ang II + BLM for 3 days. **J** Immunoblotting analysis of senescent markers (p53, p16, and p21) in WT and KO VSMCs treated by Ang II + BLM for 3 days. **K** Gene expression of SASP factors (*Il-1b, Il-6, Cxcl1, Ccl2, Icam1*, and *Gdf15*) in WT and KO VSMCs treated by Ang II + BLM for 3 days. Data were presented as mean ± SEM. *N* = 6 biological replicates. An unpaired Student's *t*-test was used. P-AAA, PPE + BAPN-induced AAA.

GSDME in VSMCs, but not in myeloid cells, mediates senescence and promotes AAA development

To identify the specific cell type responsible for GSDME-mediated pyroptosis in response to AAA, a mouse model was created. This model carried a transcriptional STOP element (3×SV40-PolyA) flanked by loxP (*loxP-Stop-loxP*, LSL) upstream of the ATG start codon of the *Gsdme* gene, as previously described (Fig. S9A)[36]. The *Gsdme*$^{\text{Stop/Stop}}$ mice were crossed with either *SMMHC*-Cre$^{\text{ERT2}}$ or *Lysm*-Cre mice to generate *Gsdme*$^{\text{Stop/Stop}}$; *SMMHC*-Cre$^{\text{ERT2}}$ (referred to as *Gsdme*$^{\text{SR}}$) or *Gsdme*$^{\text{Stop/Stop}}$; Lysm-Cre mice (referred to as *Gsdme*$^{\text{MR}}$), respectively, achieving tissue-specific rescue of GSDME in either VSMCs or myeloid cells (Fig. S9B, C), as confirmed by qPCR and immunoblotting (Fig. S9D, E). Subsequently, *Gsdme*$^{\text{WT/WT}}$, *Gsdme*$^{\text{Stop/Stop}}$, *Gsdme*$^{\text{SR}}$, and *Gsdme*$^{\text{MR}}$ mice were subjected to an AAA model.

Compared with *Gsdme*$^{\text{WT/WT}}$ mice, *Gsdme*$^{\text{SR}}$ mice had a comparable survival period, while *Gsdme*$^{\text{Stop/Stop}}$ and *Gsdme*$^{\text{MR}}$ mice exhibited significantly prolonged survival (Fig. 7A). Ultrasound imaging showed that during AAA progression, the maximal aortic diameter expanded significantly more slowly in *Gsdme*$^{\text{Stop/Stop}}$ and *Gsdme*$^{\text{MR}}$ mice, whereas *Gsdme*$^{\text{SR}}$ mice exhibited no such attenuation (Fig. 7B). Similar to GSDME-KO mice, *Gsdme*$^{\text{Stop/Stop}}$ and *Gsdme*$^{\text{MR}}$ mice displayed significantly smaller aorta weight, while *Gsdme*$^{\text{SR}}$ mice had comparable aorta weight to *Gsdme*$^{\text{WT/WT}}$ mice (Fig. 7C). EVG staining demonstrated that *Gsdme*$^{\text{Stop/Stop}}$ and *Gsdme*$^{\text{MR}}$ mice, but not *Gsdme*$^{\text{SR}}$ mice, retained more elastin fibers (Fig. 7D). Immunohistochemistry showed that both CCR2 and MMP2 were inhibited in the lesion vascular wall of *Gsdme*$^{\text{Stop/Stop}}$ and *Gsdme*$^{\text{MR}}$ mice but not in *Gsdme*$^{\text{SR}}$ mice (Fig. 7E, F). The mRNA levels of SASP secretome factors (*Il-1β, Il-6, Cxcl1, Ccl2, Icam1*, and *Gdf15*) exhibited similar changes (Fig. 7G). These findings suggest that rescuing GSDME in VSMCs, rather than myeloid cells, reproduces the induced senescence in AAA, as well as the AAA development.

Senolytic therapy alleviates GSDME-dependent AAA progression by targeting VSMC senescence

Given the implication of senescence in AAA development in these mice, we evaluated whether senolytic therapy with dasatinib plus quercetin (D + Q) could mitigate the accelerated AAA progression driven by GSDME-mediated pyroptosis. We initially assessed the effects of D + Q on the lesion vasculature at an early stage (1 week post P-AAA induction), characterized by molecular changes preceding morphological aneurysm formation. Immunohistochemistry analysis showed that in Gsdme$^{\text{SR}}$ mice, D + Q treatment significantly reduced vascular senescence, evidenced by decreased protein levels of pro-senescence molecules and SASP factors in the lesion vascular wall (Fig. S10A–F). At the onset of AAA formation (four weeks post P-AAA induction), D + Q therapy led to reduced SA-β-gal staining intensity in AAA lesion vasculature in Gsdme$^{\text{SR}}$ mice (Fig. 8A). Flow cytometry analysis revealed a remarkable decrease in the proportion of senescent cells (p16$^+$ and p21$^+$) specifically in VSMCs isolated from AAA lesions following D + Q treatment (Fig. 8B, C). Notably, D + Q therapy partially inhibited the increase in aneurysm diameter and aortic weight in Gsdme$^{\text{SR}}$ mice, along with a reduction in the proportion of large aneurysms (>4 mm) (Fig. 8D, E). Importantly, D + Q treatment did not directly affect GSDME activation, indicating that its therapeutic effect occurs downstream or independent of GSDME cleavage (Fig. S11A). Consistently, D + Q exhibited a comparable protective effect in Gsdme$^{\text{WT/WT}}$ mice (Fig. S11B). D + Q treatment also suppressed the mRNA expression of SASP factors (Fig. 8F), improved vascular structure, and increased elastin fiber content in AAA lesion vasculature of *Gsdme*$^{\text{SR}}$ mice (Fig. 8G, H). Moreover, D + Q inhibited protein levels of CCL2 and MMP2 in the vascular wall (Fig. 8I, J). Interestingly, D + Q treatment did not further ameliorate AAA pathologies in *Gsdme*$^{\text{Stop/Stop}}$ mice (Fig. 8A–J). These findings indicate that the pro-senescence effect of GSDME in VSMCs is a key driver of AAA development, and that senolytic therapy targeting senescent cells can effectively mitigate AAA progression in the presence of GSDME-mediated senescence.

Discussion

This study unveils four significant findings. Firstly, we discovered cleavage of GSDME and activation of GSDME-mediated pyroptosis in AAA lesion tissue from mouse models or patients. Deletion of GSDME was found to impede AAA development in mice. Secondly, we revealed that deletion of GSDME hindered the shift toward a pro-senescent state in composed cells within AAA vasculature. Thirdly, we demonstrated that reinstating GSDME expression in VSMCs, rather than myeloid cells, in mice with a GSDME-deficient background replicated the pro-senescent state in AAA lesion tissue and promoted AAA development. Lastly, senolytic therapy relieved AAA pathologies in mice with VSMC-specific rescue of GSDME. Together, these findings underscore the importance of GSDME in AAA progression by inducing VSMC senescence (Fig. 9).

Although pyroptosis has been established as a key contributor to AAA pathogenesis by our group and others[15,16,18], the specific molecular mechanisms governing pyroptotic execution in AAA remain incompletely characterized. While GSDMD, the canonical pyroptosis executor, was shown to promote AAA progression through modulation of serum putrescine levels[17], our integrated multi-omics approach - incorporating single-cell RNA sequencing, experimental models, and human tissue analyses - reveals GSDME as the predominant gasdermin family member transcriptionally upregulated in AAA lesions, with particularly robust expression in VSMCs. This cell-type-specific expression pattern is remarkable: GSDMD expression is primarily restricted to immune cell populations (including monocytes/macrophages, T cells, and NK cells), while GSDME demonstrates significant enrichment in VSMCs and fibroblasts. The molecular basis for this dichotomy is further evidenced by the >10-fold higher expression of caspase-3 (the primary activator of GSDME) relative to caspase-1 (the main activator of GSDMD) in AAA lesions, strongly suggesting that the caspase-3-GSDME axis represents the dominant pyroptotic pathway in vascular remodeling. These findings align with the established functional specialization of these executors: GSDMD plays a critical role in immune cell-mediated host defense[30,31], whereas GSDME serves as a key regulator of cell death modality transitions in parenchymal

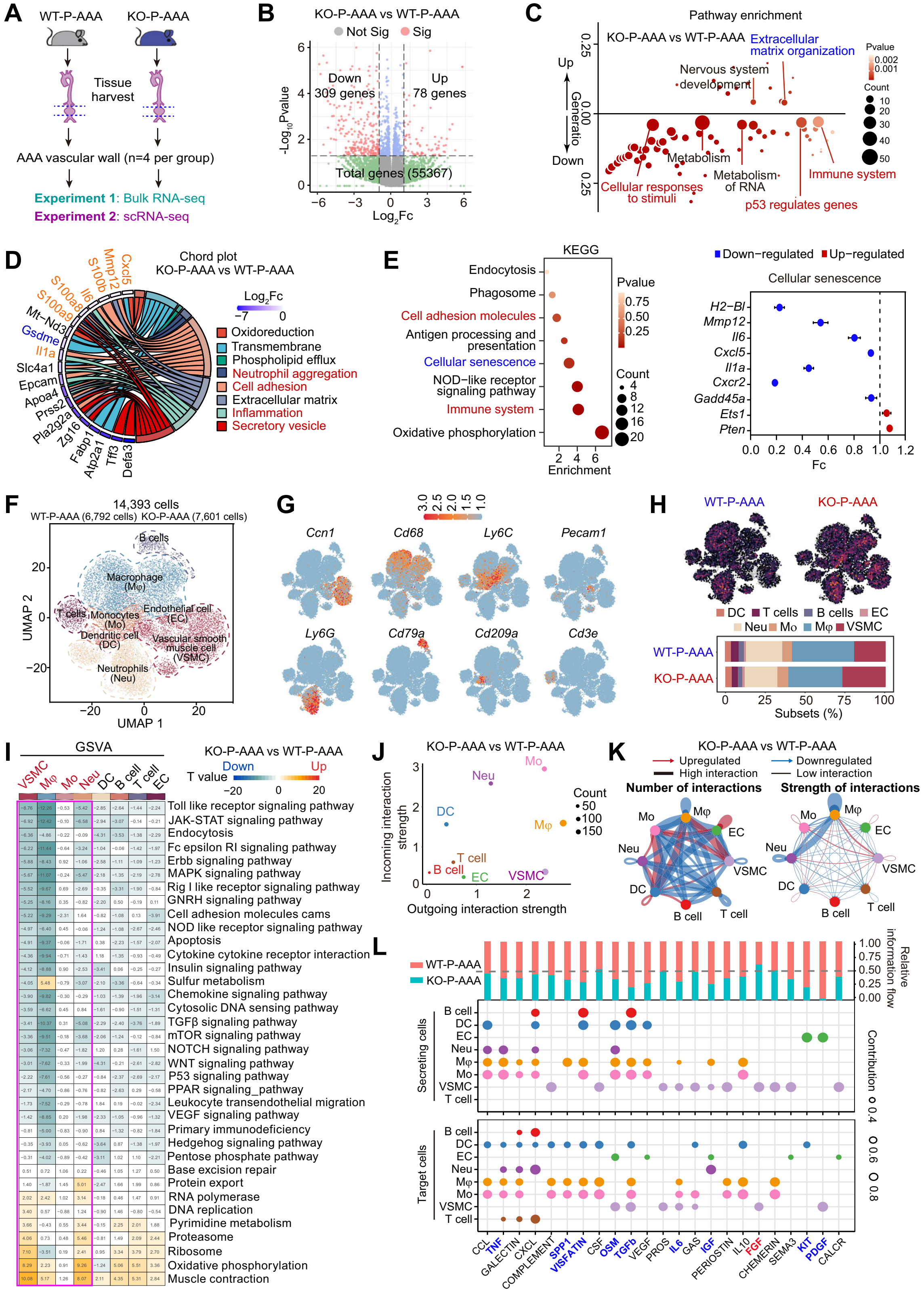

tissues[9,37], capable of shifting between apoptotic and pyroptotic pathways - a phenomenon we previously characterized in liver injury models[11]. Notably, structural differences further distinguish these pathways, particularly the presence of Thr6 in GSDME (but not GSDMD), which undergoes AMPK-mediated phosphorylation to suppress pyroptosis, a regulatory mechanism conserved in GSDMA, GSDMB, and GSDMC[38,39].

One of the most significant findings of this study was the essential regulatory action of GSDME on senescence. In our experiments, it was observed that overwhelming blue-stained SA-β-gal-positive senescent cells accumulated in AAA lesion vasculature, providing direct evidence for the involvement of senescence in AAA. As expected, deletion of GSDME almost totally abolished the triggered senescent markers and SASP secretome in AAA lesion vasculature. Using multiple flow

Fig. 5 | Bulk RNA-seq and scRNA-seq transcriptional profiling demonstrate that GSDME deficiency alleviates senescence in vascular cells of the AAA lesion. **A** Representative experimental design of combined bulk RNA-seq and scRNA-seq analyses in the AAA lesion vasculature of WT and KO mice. **B** Volcano plot demonstrates differentially expressed genes (DEGs) between the AAA lesion vasculature of WT and KO mice. **C** Signaling pathway enrichment analysis within DEGs of the AAA lesion vasculature of WT and KO mice. **D** The chord plot demonstrates the changed biological processes in comparison of the AAA lesion vasculature of WT and KO mice. **E** KEGG analysis demonstrates the changed pathway in comparison of the AAA lesion vasculature of WT and KO mice. *N* = 4 biological replicates. **F** scRNA-seq reveals the cell types in the AAA lesion vasculature of WT and KO mice. **G** UMAP plot demonstrates the marker genes of specific types of cells, including VSMCs (*Ccn1*), neutrophils (*Ly6G*), T cells (*Cd3e*), endothelial cells (*Pecam1*), B cells (*Cd79a*), monocytes (*Ly6C*), macrophages (*Cd68*), and dendritic cells (*Cd209a*) in the AAA lesion vasculature of WT and KO mice. **H** UMAP plot shows the proportions of each cell cluster in the AAA lesion vasculature of WT and KO mice, respectively. **I** Heatmap presents enriched pathways in each cell cluster via gene set variation analysis (GSVA). **J** Scatterplot showing the contribution of each cell type to the incoming and outgoing interaction strength in the AAA lesion vasculature. The size of the dots is proportional to the total number of incoming and outgoing signaling pathways associated with a cell type. **K** Circle plot demonstrating the communicative signaling network in the AAA lesion vasculature. The thickness of the lines represents signaling strength; the arrows point toward signal-receiving cells. **L** Dot plot summarizing the signal-sending and -receiving cells for each listed pathway mediated by secreted or cell surface molecules in the AAA lesion vasculature. The size of the dots is proportional to the contribution of a cell type to a specific pathway. The inhibited secreted factors in the KO-AAA vasculature were colored blue, whereas the induced ones were colored red. P-AAA refers to PPE + BAPN-induced AAA. DESeq2 tests (**B**–**E**) were performed. Data were presented as mean ± SEM.

cytometry, we further found that GSDME deficiency tremendously limited the infiltration of Mφ/Mo within the AAA lesion vascular wall. Specifically, the number of inflammation-resolving Mφ/Mo, including TIM4$^+$ TRM[25] and the reparative Ly6C^{lo} Mo (non-classical Mo)[40], was enhanced in AAA tissue of GSDME-KO mice. Meanwhile, reduced frequencies of MHCII$^+$ Mφ with superior antigen-presentation capacity[26] and pro-inflammatory Ly6C^{hi} Mo (classical Mo) were observed in AAA tissue of GSDME-KO mice. These findings outlined the promoting effects of GSDME on vascular immune and inflammation in AAA progression. As there has been plenty of evidence showing the critical contribution of IL-1 family/IL-18 signaling in senescence[41–43], and GSDME is an upstream controller of IL-1 family/IL-18 signaling, we propose that GSDME in VSMCs may be a 'master switch' of senescence in AAA.

As caspase-3 bridges apoptosis and pyroptosis, the Caspase-3-GSDME signaling pathway elegantly controls the balance between apoptosis and pyroptosis. In the condition of GSDME being blocked, caspase-3 would shift the cell death mode to 'apoptosis', which is the other end of the scale. Indeed, a recent research designed a naturally inspired 'synpoptosis' circuits that proteolytically regulate engineered executioner proteins based on the GSDM family to select a specific mode of cell death between apoptosis and pyroptosis[44]. This seems to raise another key question: whether 'apoptosis' might not induce senescence. Historically, apoptosis has been regarded as the sole pathway of RCD. Yet, research over the last two decades challenges this assertion[45]. Apoptosis is now considered immunologically silent or 'cold' RCD, while pyroptosis is immunologically 'hot' RCD involving a massive release of DAMPs, triggering remarkable activation of the immune system and inflammation. The complex relationship between GSDME and apoptosis/pyroptosis balance in various pathological conditions, not limited to AAA, is a rather interesting issue that needs to be intensively studied.

Our bulk RNA-seq data indicate that both immune response and senescence in AAA lesion tissue were largely inhibited by GSDME deletion. Further evidence from scRNA-seq analysis provided cell-type-specific insights into the characteristics of 'immunosenescence'. The proportion of the contractile VSMCs subgroup was rather low in AAA lesion tissue from both types of mice (<5%), suggesting a scarcity of normal VSMCs in AAA lesion tissue. Additionally, the proportions of Mφ-like and fibroblast-like VSMCs subgroups, representing terminal differentiation state VSMCs in AAA, were notably decreased by GSDME deletion. Consistent with the condition in VSMCs, the AAA lesion tissue in KO mice exhibited a lower proportion of immunostimulatory Mφ and higher proportions of immunosuppressive Mφ or TRM. TRM, a specific group of embryonic-derived Mφ with tissue regeneration and anti-senescence characteristics[46], has recently gained attention for their presence in aortic aneurysm[47]. Our results suggest that GSDME-dependent pyroptosis plays a significant role in the decline of TRM in AAA. Similar effects of GSDME were observed in neutrophils, as a deficiency in GSDME significantly impeded the transition of neutrophils toward a *Cxcr2*$^+$ immunosenescence status[32]. Results from cell-cell communication network analysis in scRNA-seq also support this conclusion, demonstrating that the AAA lesion tissue in KO mice had a significantly lower SASP secretome. To mechanistically probe whether GSDME-mediated pyroptosis promotes AAA by inducing VSMC senescence and subsequent SASP, we employed the senolytic agent D + Q, which has been shown to mitigate age-related disorders in aged mice[48] and reduce AAA development[49]. Treatment with D + Q ameliorated AAA and senescence phenotypes in mice with intact *Gsdme* expression in VSMCs but failed to confer additional benefit in mice with global Gsdme deletion. These findings support the notion that GSDME promotes AAA primarily through inducing VSMC senescence and the associated SASP program. Although the therapeutic potential of D + Q was not the primary focus of our study, our data further corroborate its value as a promising intervention for AAA, particularly in contexts where pyroptosis-driven senescence contributes to disease progression. Future studies exploring D+Q's clinical applicability, including dose optimization and patient stratification based on senescence biomarkers, could help translate these findings into therapeutic strategies.

Overall, this study has unveiled the pivotal role of GSDME in propelling the progression of AAA by fostering vascular senescence, indicating that targeting GSDME may be a promising strategy for the treatment of AAA.

Methods

Animals

Wildtype (WT) C57BL/6J mice were purchased from Sino-British SIPPR/BK Lab Animal Ltd. (Shanghai, China). *Gsdme* global knockout (KO) mice and *Gsdme*$^{stop/stop}$ mice were described in our previous study[11,12,36]. ApoE$^{-/-}$ mice were obtained from Cyagen Biosciences (Guangzhou, China). Lysm-Cre mice (B6.129P2-Lyz2tm1(cre)Ifo/J, #004781) were obtained from The Jackson Laboratory. SMMHC-Cre^{ERT2} mice (B6.FVB(Cg)-Tp(X)1SoffTg (Myh11-icre/ERT2)1Soff, #019079) that express a tamoxifen-inducible Cre recombinase under the regulatory sequences of smooth muscle *Myh11* promoter, inserted into the Y chromosome, were obtained from The Jackson Laboratory. Gsdme$^{stop/stop}$; Lysm-Cre mice were generated by crossbreeding Gsdme$^{stop/stop}$ mice with *Lysm*-Cre mice. Gsdme$^{stop/stop}$; SMMHC-CreERT2 mice were generated by crossbreeding Gsdme$^{stop/stop}$ mice with SMMHC-CreERT2 mice and induced by tamoxifen (75 mg/kg/d, T5648, Millipore Sigma) by intraperitoneally injection for 5 consecutive days. All animal protocols were reviewed and approved by the Institutional Animal Care and Use Committee of Shanghai Tenth People's Hospital of Tongji University and followed the Principles of the Guide for the Care and Use of Laboratory

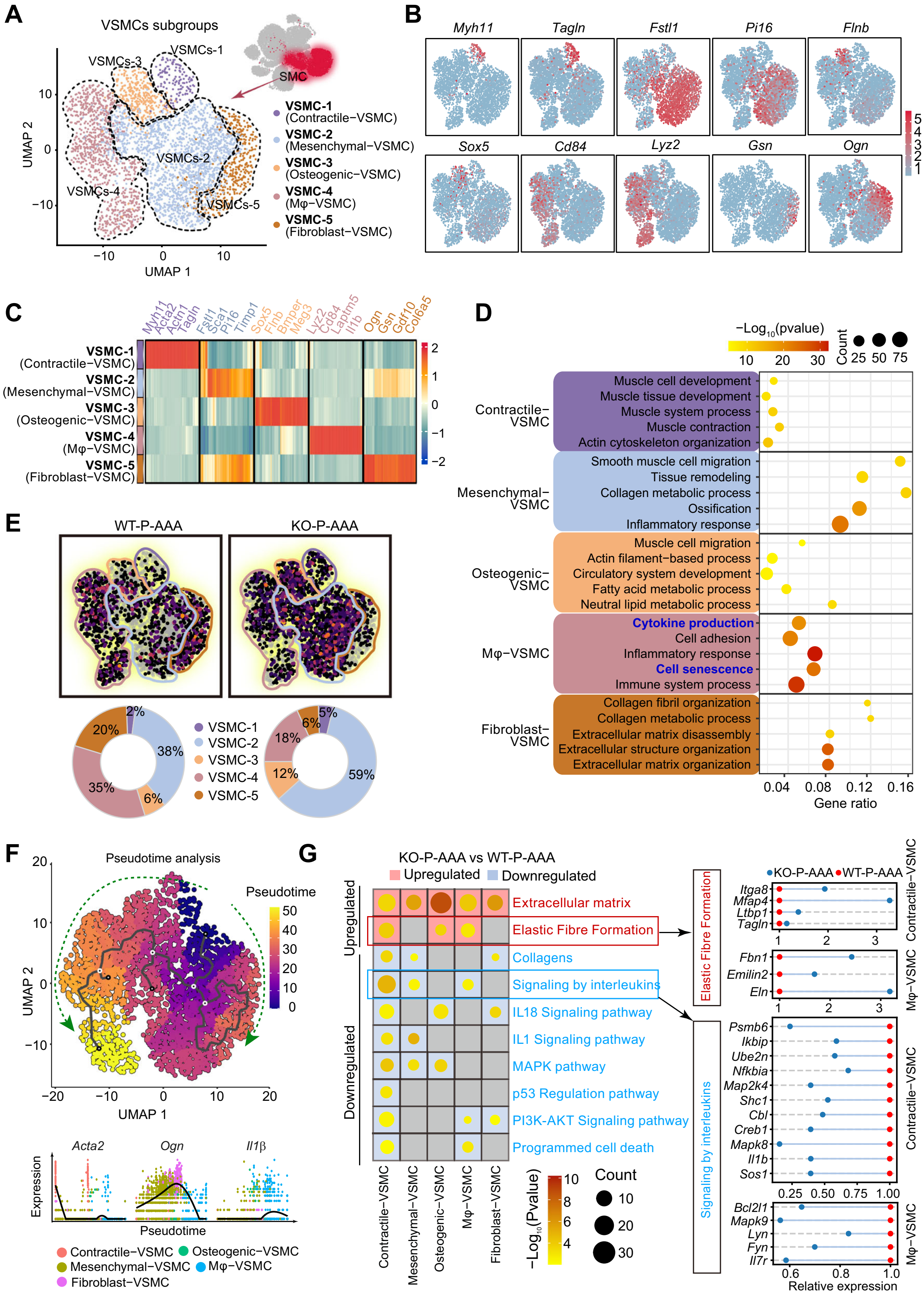

Animals published by the US National Institutes of Health (NIH Publication 8th edition, update 2011). All mice were kept under the specific pathogen-free conditions and were housed in a temperature-controlled (23 ± 2 °C) and humidity-controlled (40 ± 5%) environment with access to water and diet, under a 12 h/12 h-light/dark cycle. Male mice (8–12 weeks old) were used, except for females in Supplementary Fig. 3B.

AAA mouse models

Two types of AAA mouse models were used. The first AAA model was induced by peri-adventitial incubation of porcine pancreatic elastin (PPE)[50] plus β-aminopropionitrile monofumarate (BAPN), a lysyl-oxidase inhibitor with potent elastin degradation activity[22]. The mice were anesthetized (pentobarbital, 40 mg/kg, i.p) and the abdominal cavity was opened. Then, the peri-aorta adipose was carefully removed,

Fig. 6 | GSDME regulates the reprogramming of VSMCs toward a pro-senescent state in AAA lesions. **A** UMAP of subgroups of VSMCs. VSMCs are further categorized into contractile VSMCs (VSMCs-1, *Myh11*$^+$*Acta2*$^+$*Tagln*$^+$*Actn1*$^+$), mesenchymal-like VSMCs (VSMCs-2, *Fstl1*$^+$*Sca1*$^+$*Pi16*$^+$*Timp1*$^+$), osteogenic-like VSMCs (VSMCs-3, *Sox5*$^+$*Flnb*$^+$*Bmper*$^+$*Meg3*$^+$), Mφ−like VSMCs (VSMCs-4, *Lyz2*$^+$*Cd84*$^+$*Laptm5*$^+$*Il1b*$^+$) and fibroblast−like VSMCs (VSMCs-5, *Gsn*$^+$*Ogn*$^+$*Gdf10*$^+$*Col6a5*$^+$). **B** UMAP of major marker genes for clustering of VSMCs subgroups. **C** Heatmap displaying the highly expressed genes in each VSMC subgroup. The VSMCs were further grouped according to these genes. **D** Biological functions enriched in the five VSMC subgroups. **E** UMAP and pie plots illustrating the differing proportions of VSMC subgroups between the AAA lesion vasculature of WT and KO mice. **F** Pseudotime trajectory analysis of VSMC subgroups and feature plots of expression distribution for *Acta2* (marker of contractile VSMCs), *Ogn* (marker of fibroblast-like VSMCs), and *Il1b* (marker of Mφ-like VSMCs) in the differentiation trajectory. **G** Integrative functional enrichment analysis showing the upregulated and downregulated biological processes and signaling pathways in VSMC subgroups of KO-AAA vasculature compared with WT-AAA vasculature. Wilcoxon tests were performed in (**D**) and (**G**).

and a sterile gauze presoaked with PPE (12 U/mL, E1250, Sigma-Aldrich) was used to surround the infrarenal abdominal aorta for 15 min as described previously[27]. The gauze was removed before closing the surgical incision, and the mice were given water containing β-BAPN (1%) for 28 days[51]. The second AAA was induced by infusion of Ang II via subcutaneously implanted Osmotic mini-pump (1000 ng/kg/min, 05-23-0101, Sigma-Aldrich) for 28 days as previously described[52].

Drug administration

Quercetin and dasatinib were purchased from Sigma-Aldrich. Dasatinib (5 mg/kg) and quercetin (50 mg/kg) were dissolved and administered via intraperitoneal injection three times a week for four weeks[53].

Human AAA samples

Human aortic tissue was collected in compliance with the Declaration of Helsinki. The presence of AAA was confirmed at the time of surgery by experienced cardiothoracic surgeons, and the clinical phenotype diagnosis was confirmed using standard histopathology at the Shanghai Changzheng Hospital or Shanghai Tenth People's Hospital. AAA tissue was collected during surgery from patients who had undergone aorta replacement or stent implantation of the aorta. Normal artery samples, such as those from the internal mammary artery used for coronary artery bypass grafting, were also collected. The study was approved by the Ethics Committee of the Shanghai Changzheng Hospital (2018SL047) or Shanghai Tenth People's Hospital (No. 23KY31). Informed consent was obtained from the participant. Patient information is summarized in Supplementary Table 2.

In vivo ultrasound imaging analysis

In vivo ultrasound imaging of abdominal aortic morphology was conducted using a high-frequency ultrasound system (VINNO6LAB, Suzhou, China) with simultaneous longitudinal and cross-sectional acquisition. Mice were maintained under continuous isoflurane inhalation anesthesia (1.5–2% in oxygen) with a stable heart rate (400–500 beats per minute). A 15-MHz linear array transducer (VINNO X10-23L) was used to measure both maximal outer diameter in longitudinal views and luminal area in cross-sectional views. Abdominal aortic aneurysm was defined as either a ≥50% increase in maximal diameter or a ≥100% expansion in cross-sectional area relative to baseline measurements, consistent with established diagnostic criteria.

Blood pressure measurements

Blood pressure in mice was measured using a noninvasive tail-cuff system (ALC-NIBP Systems, Shanghai Alcott Biotech CO., LTD., Shanghai, China) four weeks after Ang II infusion, following the manufacturer's protocol.

Primary culture of mouse VSMCs

Primary aortic vascular smooth muscle cells (VSMCs) were isolated from WT and Gsdme global knockout mice and cultured as described in our previous studies[2,27]. Briefly, the aortae of mice were harvested from the arcus aortae to the iliac bifurcation, cleaned off fibro and perivascular adipose tissue under a dissecting microscope. The aortic tissues were cut into pieces (2 mm * 2 mm), added to 6-well plates containing 1 ml cultured media, and grown for seven days to allow the cells to emerge. The primary mouse VSMCs were cultured in a low serum (5% fetal bovine serum) mammal VSMCs-specific medium (DMEM/F-12, Dulbecco's Modified Eagle Medium/Nutrient Mixture F-12) supplemented with 1% penicillin-streptomycin (15140122, Gibco) at 37 °C in a humidified incubator with 5% CO_2.

Isolation of bone marrow primary macrophages (BMPMs)

BMPMs were isolated from the femurs of euthanized 6- to 12-week-old mice as previously described[54]. Briefly, the tibia and femur were dissected after the mice were immersed in 70% ethanol for surface sterilization, followed by three washes with PBS. Bone marrow was flushed out with 2% FBS-PBS using a 25G needle attached to a 10 mL syringe. The resulting cell suspension was filtered through a 70-µm cell strainer to remove debris. Red blood cells were lysed by incubating the cells in red blood cell lysis buffer for 2 min at 4 °C. Cells were then centrifuged at 300 × *g* for 5 min and resuspended in culture medium. To enrich for adherent myeloid cells, the suspension was plated and incubated at 37 °C for 2 h, after which non-adherent cells were removed by washing with PBS. The adherent cells were subsequently collected for RNA and protein extraction and further analyses.

Cell culture and treatment

Primary human aortic smooth muscle cells (HUASMC) (Cat#6110) were purchased from the ScienCell Research Laboratories, Inc. THP-1 cells (Cat# TIB-202) were purchased from the American Type Culture Collection. Cells were cultured in DMEM (Solarbio, China, Cat#12100-500) containing 10% FBS,100 U/ml of penicillin, and 100 µg/ml of streptomycin. Followed by continuous stimulation with Ang II (0.1 µM, #A6778, Sigma) and BLM (100 nM, S1214, Selleck), cells were obtained and lysed, and proteins were extracted for subsequent experiments.

Enzyme-linked immunosorbent assay (ELISA)

The concentration of IL-18, IL-1β, and HMGB1 in aortae was performed using the mouse IL-18 ELISA Kit (DY7625-05, R&D Systems), the mouse IL-1b ELISA Kit (MLB00C, R&D Systems), mouse HMGB1 ELISA Kit (EEL102, Invitrogen) following the manufacturer's instructions.

Preparation of a single-cell suspension from the aorta

Single cells were isolated from the abdominal aorta of mice with AAA for flow cytometry as described previously[55]. Briefly, mice were killed, and the aortae were perfused with PBS to remove all traces of blood. Aortae were isolated and cut into small pieces, and then incubated in Hank's buffered salt solution (HBSS) containing collagenase I digestion enzymes (0.5 mg/ mL, Worthington) for 80 min at 37 °C at 25 g in PythoNTM-Tissue Dissociation (Singleron, Hefei, China)[56]. After incubation, the Same volume of 10% FBS was added to stop digestion, and cell suspensions were filtered through a 70 µm cell strainer. After that, cell suspensions were centrifuged for 10 min at 350 × *g* at 4 °C and resuspended with HBSS.

Multiplex flow cytometry and high-dimensional analysis

Immune cells (CD45$^+$ cells) within the vascular wall were isolated from aorta single-cell solution using the Magnetic Activated Cell Sorting

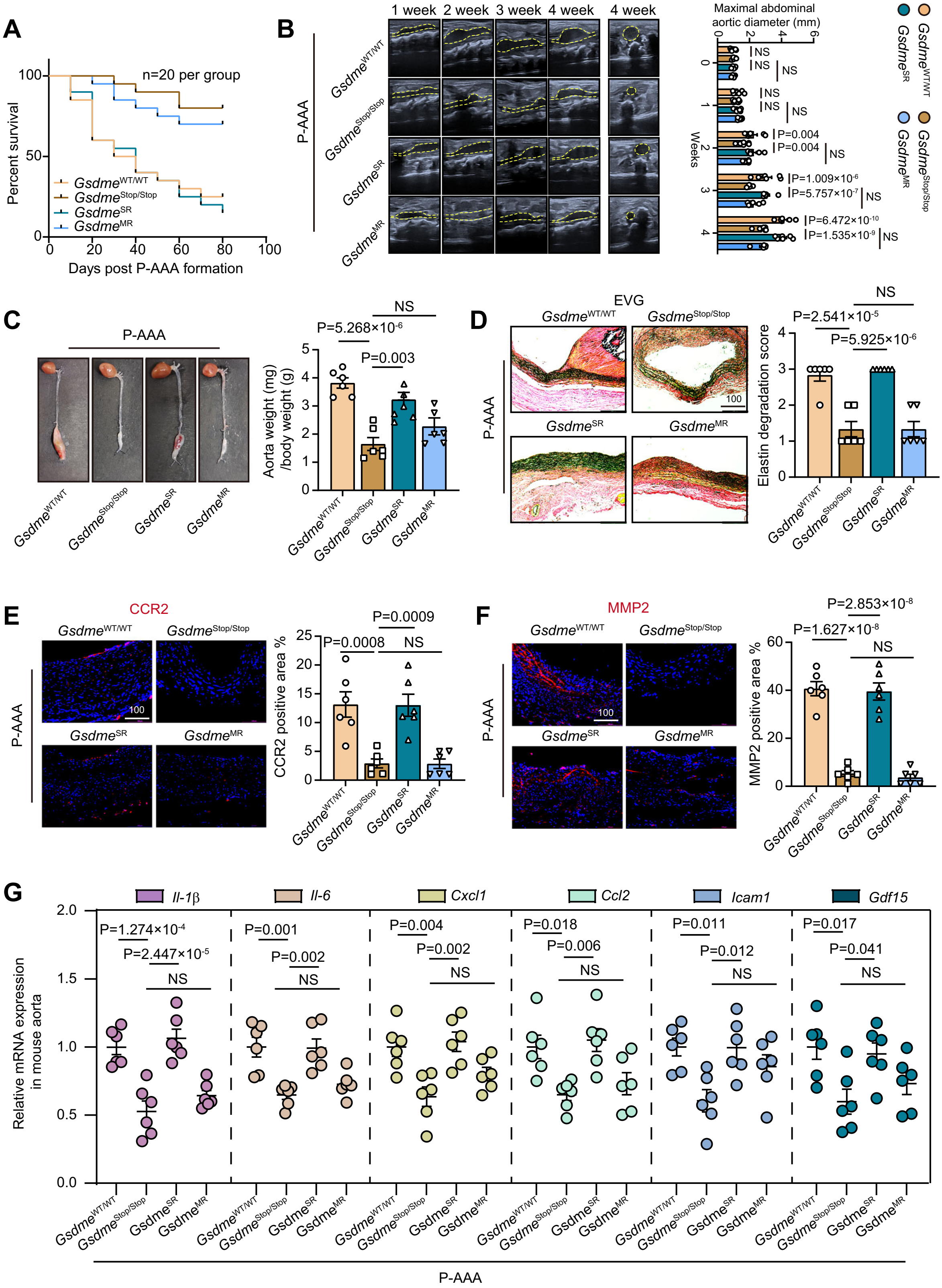

system[57] (Miltenyi Biotec, Bergisch Gladbach, Germany) with CD45 MicroBeads (catalog no. 130-052-301). The isolated CD45$^+$ cells were pre-incubated with 0.025 µg of TruStain FcX™ anti-CD16/32 antibody (BioLegend) for 10 min on ice to block Fc receptors. Then, the cells were stained with appropriate antibodies at 4 °C in the dark for 45 min. Dead cells were excluded using propidium Iodide (BD Biosciences) staining. The cells were clustered using multiplexing flow cytometry with antibodies (1:50 dilution) against CD45, CD11b, Ly6G, F4/80, TIM4, MHCII, and Ly6C. Samples were acquired using a CytoFLEX S (Beckman) and analyzed with high-dimensional analysis using an unbiased nonlinear dimensionality reduction algorithm (t-distributed stochastic neighbor embedding, t-SNE) in FlowJo software (version 10; Tree Star). The list of antibodies for flow cytometry is listed in Supplementary Table 2.

Fig. 7 | GSDME in VSMCs mediates senescence in AAA. A Survival curve of *Gsdme*$^{WT/WT}$, *Gsdme*$^{Stop/Stop}$, *Gsdme*^{SR}, and *Gsdme*^{MR} mice after P-AAA formation. **B** Representative images and quantification of maximal abdominal aortic diameter visualized by ultrasound of *Gsdme*$^{WT/WT}$, *Gsdme*$^{Stop/Stop}$, *Gsdme*^{SR}, and *Gsdme*^{MR} mice in the P-AAA model. **C** Representative morphology of the aorta tree of *Gsdme*$^{WT/WT}$, *Gsdme*$^{Stop/Stop}$, *Gsdme*^{SR}, and *Gsdme*^{MR} mice in the P-AAA model. **D** Representative elastin-Van-Gieson (EVG) staining and elastin degradation score in lesion vasculature of *Gsdme*$^{WT/WT}$, *Gsdme*$^{Stop/Stop}$, *Gsdme*^{SR}, and *Gsdme*^{MR} mice in the P-AAA model. Representative immunofluorescence staining and quantitative analysis of CCR2 (**E**) and MMP2 (**F**) in lesion vasculature of *Gsdme*$^{WT/WT}$, *Gsdme*$^{Stop/Stop}$, *Gsdme*^{SR}, and *Gsdme*^{MR} mice in P-AAA model. (**G**) Measurement of mRNA expression of SASP factors (*Il-1*β, *Il-6*, *Cxcl1*, *Ccl2*, *Icam1*, and *Gdf15*) in lesion vasculature of *Gsdme*$^{WT/WT}$, *Gsdme*$^{Stop/Stop}$, *Gsdme*^{SR}, and *Gsdme*^{MR} mice in the P-AAA model. Data were presented as mean ± SEM. *N* = 6 biological replicate unless indicated. Two-way ANOVA was used in (**B**). One-way ANOVA followed by Tukey's test was used in other panels. P-AAA, PPE + BAPN-induced AAA.

Determination of cell senescence and death in VSMCs

The mouse abdominal aorta was harvested and enzymatically dissociated into a single-cell suspension. Following fixation and permeabilization, cells were incubated with AF488-conjugated α-SMA antibody in the dark at 4 °C overnight. After washing and resuspension in HBSS, the cells were sequentially stained with other antibodies against p16, p21, GSDMD, or GSDME (RT, 2 h), followed by PE- or AF647-conjugated secondary antibodies (RT, 30 min). For cell death detection, the aorta single cells were stained with SYTOX dead dye (for 5 min at 4 °C) first. After centrifugation, washed, and resuspension in HBSS, the cells were fixed and permeabilized and then incubated with AF488-labeled α-SMA antibody. All samples were analyzed using a CytoFLEX S flow cytometer (Beckman Coulter), and data processing was performed with FlowJo software (v10, Tree Star).

Senescence-associated-β-galactosidase (SA-β-gal) staining

SA-β-gal activity staining was performed with a commercial kit (C0602, Beyotime Biotechnology) as described in our previous studies[2,27]. Briefly, after washing in PBS three times, aortic samples or cultured cells were fixed in an appropriate amount of β-galactosidase Staining Fixative and incubated at room temperature for 15 min. Following this, aortic samples or cultured cells were washed in PBS 3 times for 5 min at least each time and then incubated overnight at 37 °C after the staining working solution was added to fully cover the aortic tissues or cultured cells. The images were obtained with a light microscope (Leica Microsystems, Berlin, Germany) and then analyzed using ImageJ software (NIH).

Immunohistochemistry

Immunohistochemistry was performed using commercial avidin-biotin complex kits (Vectastain® Elite ABC Kit; Vector Laboratories). The 8-µm-thick aorta sections were dried at 37 °C overnight. After antigen retrieval, the endogenous peroxidase was quenched with 1% H_2O_2 for 20 min and the unspecific binding was blocked with 5% normal goat serum (#31872, Thermo) for 2 h. Then the sections were stained with primary antibodies at room temperature for 4 h. After being washed with PBS three times, the slides were then incubated with biotinylated-conjugated secondary antibodies for 1 h, and streptavidin conjugated with HRP was used to implement antigen-specific immunohistochemistry. The slides were visualized using a chromogenic substrate, diaminobenzidine, for 2 min and counterstained with hematoxylin for 2 min. Controls included omitting primary antibodies and omitting secondary antibodies (Fig. S12). Tissue sections were observed using an Olympus BX51 microscope (Olympus, Tokyo, Japan). The intensity of the positive area in immunohistochemistry was evaluated using ImageJ software. The antibodies were listed in the Supplementary Table 2.

Immunofluorescence

Tissues were fixed in 4% PFA at 4 °C overnight and dehydrated in 30% sucrose. After being embedded in OCT Compound, aortic sections (10 µm) were washed, permeabilized, and saturated with PBS, 3% BSA, 0.2% Triton X-100, and 10% Goat serum for 1 h at room temperature. The sections were incubated with primary antibodies overnight at 4 °C. The Alexa Fluor 488-conjugated antibody or the Alexa Fluor 568-conjugated antibody was used as a secondary antibody. DAPI was used to stain nuclei. The images were captured by a confocal microscope (FV1000, Olympus). The antibodies were listed in the Supplementary Table 2.

Histopathological analysis

Histopathological analyses were performed on the paraffin-embedded sections of the aortic tissues. Hematoxylin and eosin (HE), elastica-van-Gieson (EVG) were performed and examined with an Olympus BX51 microscope (Olympus, Tokyo, Japan) and analyzed with ImageJ software (NIH) to assess elastin degradation of the aorta. The extent of elastic fiber fragmentation was scored on a scale of 0 to 3 (0 = none, 1 = minimal, 2 = moderate, 3 = severe) and analyzed.

Immunoblotting

Aorta samples were lysed with RIPA lysis buffer (#P0013B, Beyotime) containing 50 mM Tris (pH 7.4), 150 mM NaCl, 1% Triton X-100, 1% sodium deoxycholate, 0.1% SDS, and protease/phosphatase inhibitor cocktails (#1046, Beyotime) in a homogenizer at 4 °C. Cultured cells were directly lysed on ice with the buffers. Proteins were run on 8–12% SDS-PAGE gels at 120 V for 1.5 h at room temperature. Then gels were transferred onto nitrocellulose membranes at 200 mA for 1 h in an ice-water bath. Membranes were blocked with 5% non-fat milk dissolved in PBST buffer (0.5% v/v Tween-20 in PBS buffer) for 2 h at room temperature. Membranes were washed (5 min × 3 times) with PBST, and incubated with primary antibodies overnight at 4 °C. The dilution of primary antibodies ranged from 1:1000 to 1:5000. After washing, membranes were incubated with secondary antibodies conjugated with IRDye ®800CW (Li-Cor Biosciences). Images were photographed with the Odyssey system (Li-Cor Biosciences) and then analyzed with ImageJ software (NIH). The antibodies were listed in the Supplementary Table 2.

Quantitative PCR

Total RNA of cells or tissues was extracted with TRIzol reagent (Invitrogen). The quality of RNA was assessed with a 260/280 nm absorption ratio using Nanodrop (Thermo Fisher Scientific). RNA was used only when the ratio was 1.8 ~ 2.0. After RNA concentration measurement, 2 µg RNA was used in the reverse transcription with One-Step gDNA Removal and cDNA Synthesis SuperMix (TransGen Biotech, China). Real-time quantitative PCR (qPCR) was performed using the BioRad CFX96 system (Bio-Rad Laboratories, Hercules, CA) with SYBR Premix Ex Taq Mixture (Takara, Tokyo, Japan). Each sample was determined in duplicate, and the housekeeping gene GAPDH was used as the reference gene for normalization. Primer sequences were listed in Supplementary Table 2. Cycle threshold (CT) values were recorded, and the $^{\Delta\Delta}$CT method was used to quantify fold changes of genes.

Bulk RNA sequencing

Total RNA was extracted from the tissue using TRIzol® Reagent according to the manufacturer's instructions (Invitrogen), and genomic DNA was removed using DNase I (TaKara). Then RNA quality was determined by 2100 Bioanalyser (Agilent) and quantified using the ND-2000 (NanoDrop Technologies). Libraries were size-selected for cDNA target fragments of 300 bp on 2% Low Range Ultra Agarose, followed by PCR amplified using Phusion DNA polymerase (NEB) for 15 PCR cycles. After quantification by TBS380, the paired-end RNA-seq sequencing library was sequenced with the Illumina HiSeq 4000 sequencer. For bioinformatics analyses, KEGG pathway analysis was carried out by KOBAS. The sequencing data for this study of aortic tissue from WT and GSDME-KO mice have been deposited in the NCBI

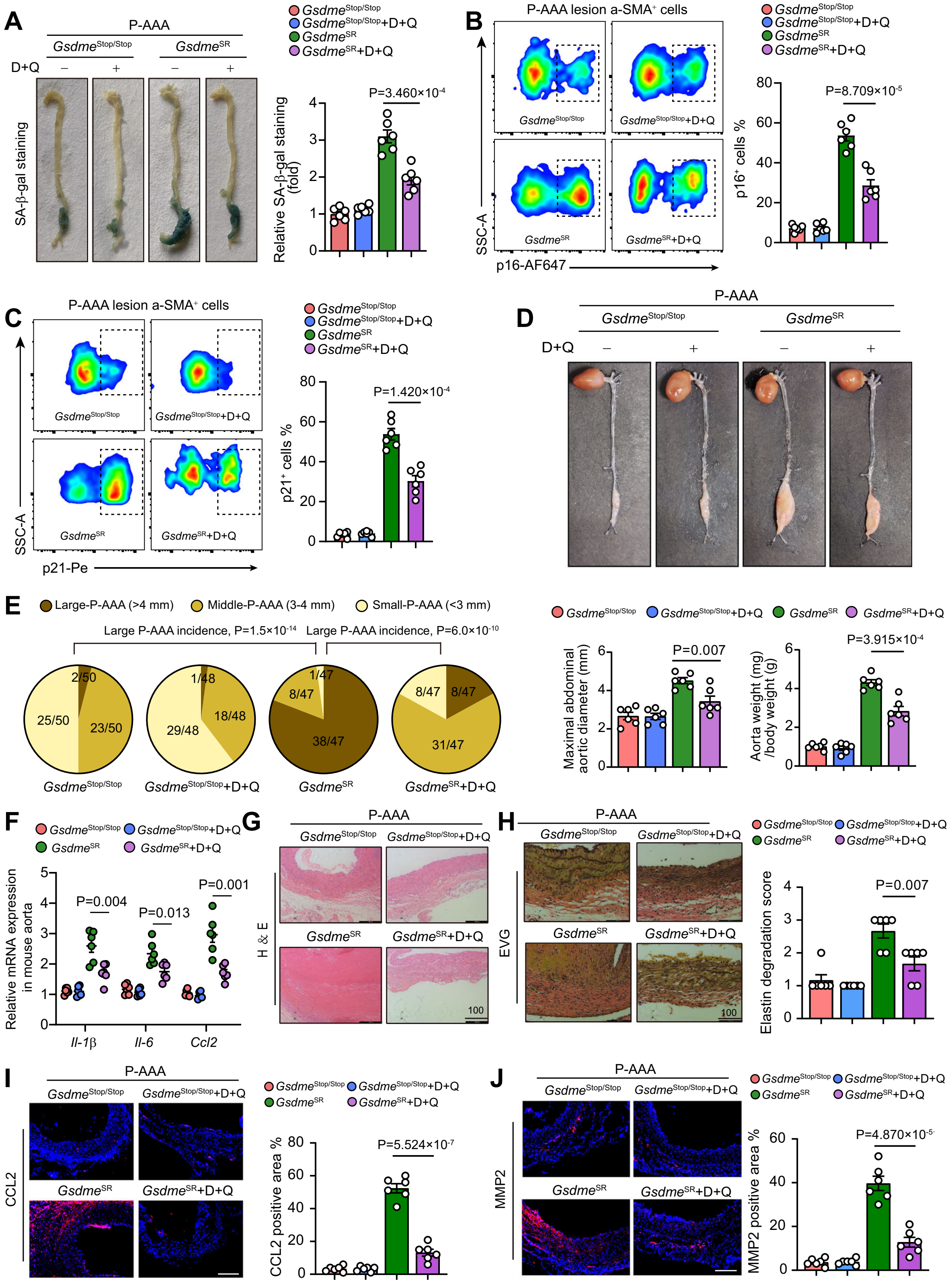

Sequence Read Archive (SRA) database and can be accessed using accession numbers PRJNA1094635.

scRNA sequencing

Aortic single cells were prepared as abovementioned and subjected to scRNA-seq (NovelBio Bio-Pharm Technology Co.) using the BD Rhapsody system as described in our previous study[54]. Single-cell capture was achieved by random distribution of a single-cell suspension across > 200,000 microwells through a limited dilution approach. Beads with oligonucleotide barcodes were added to saturation so that a bead was paired with a cell in a microwell. The cells were lysed in the microwell to hybridize the mRNA molecules to the barcoded capture oligos on the beads. Beads were collected into a single tube for reverse transcription and Exo I digestion. Upon cDNA synthesis, each cDNA molecule was

Fig. 8 | Senolytic therapy ameliorates AAA pathologies in mice with VSMC-specific rescue of GSDME. **A** SA-β-gal staining of the AAA lesion aorta tree of *Gsdme*$^{Stop/Stop}$ and *Gsdme*^{SR} mice treated by senolytic therapy of dasatinib plus quercetin (D + Q) or vehicle control. The AAA lesion vasculatures were blue-stained. **B** Flow cytometry of p16-positive senescent cells in a-SMA$^+$ cells from AAA lesion vasculatures of *Gsdme*$^{Stop/Stop}$ and *Gsdme*^{SR} mice treated by senolytic therapy of D + Q or vehicle control. **C** Flow cytometry of p21-positive senescent cells in a-SMA$^+$ cells from AAA lesion vasculatures of *Gsdme*$^{Stop/Stop}$ and *Gsdme*^{SR} mice treated by senolytic therapy of D + Q or vehicle control. **D** Representative morphology and quantitative analyses of maximal abdominal aortic diameter and aorta weight in *Gsdme*$^{Stop/Stop}$ and *Gsdme*^{SR} mice treated by senolytic therapy of D + Q or vehicle control. **E** Comparison of the incidence of large P-AAA in *Gsdme*$^{Stop/Stop}$ and *Gsdme*^{SR} mice treated by senolytic therapy of D + Q or vehicle control. The reported numbers (50, 48, 47, and 47 for the four groups) represent the cumulative use across multiple experimental procedures (molecular assays, flow cytometry, histopathology, and survival analyses). **F** The mRNA expression of SASP factors (*Il-1β*, *Il-6*, and *Ccl2*) in lesion vasculature of *Gsdme*$^{Stop/Stop}$ and *Gsdme*^{SR} mice treated by senolytic therapy of D + Q or vehicle control. **G** Representative H&E staining in lesion vasculature of *Gsdme*$^{Stop/Stop}$ and *Gsdme*^{SR} mice treated by senolytic therapy of D + Q or vehicle control. **H** Representative EVG staining and elastin degradation score in lesion vasculature of *Gsdme*$^{Stop/Stop}$ and *Gsdme*^{SR} mice treated by senolytic therapy of D + Q or vehicle control. Representative immunofluorescence staining and quantitative analysis of CCL2 (**I**) and MMP2 (**J**) in lesion vasculature of *Gsdme*$^{Stop/Stop}$ and *Gsdme*^{SR} mice treated by senolytic therapy of D + Q or vehicle control. Data were presented as mean ± SEM. *N* = 6 biological replicate unless indicated. Chi-squared test was performed in (**E**), and Unpaired Student's *t*-tests were used in other panels. P-AAA, PPE + BAPN-induced AAA.

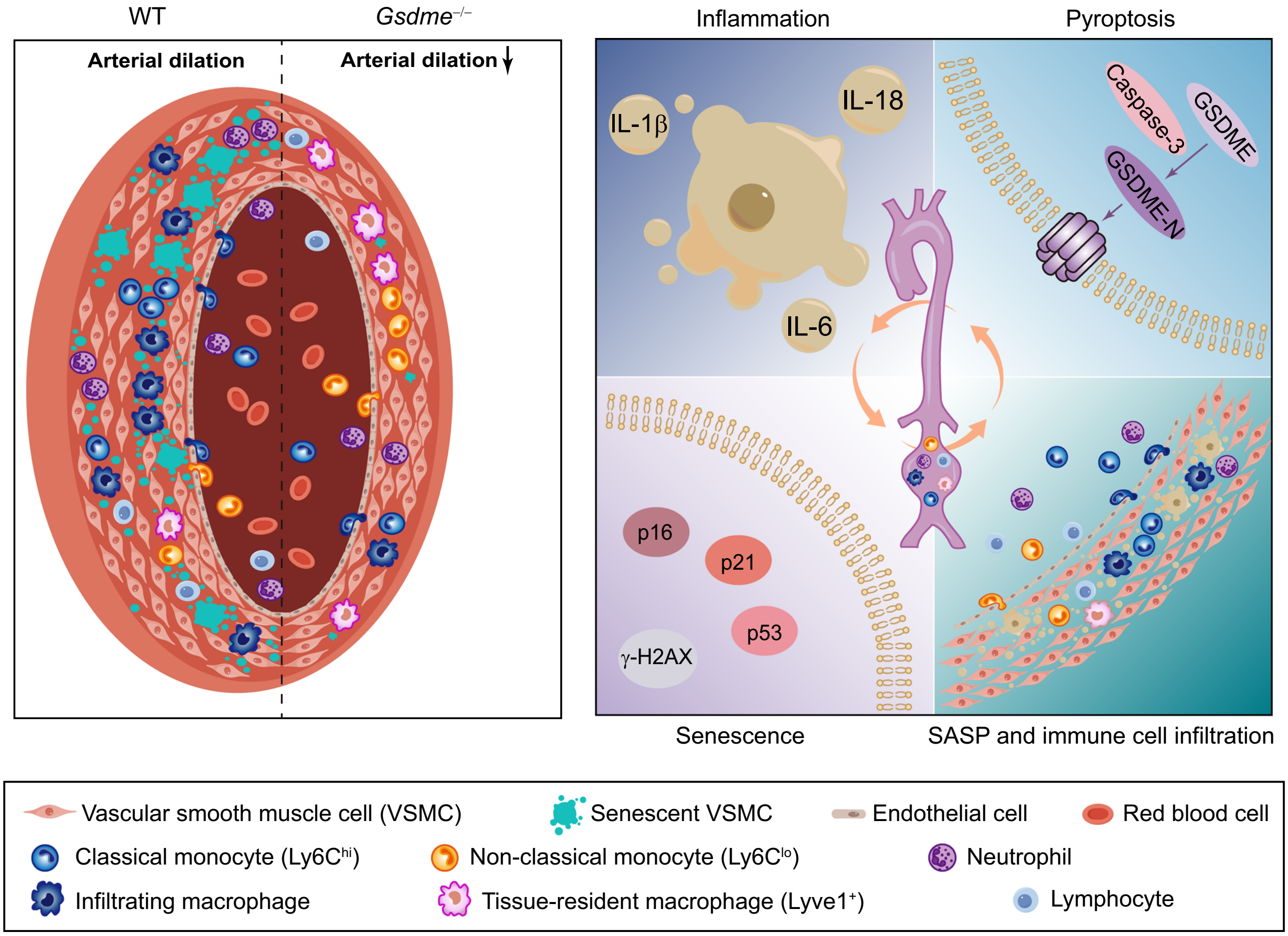

Fig. 9 | Proposed working model illustrating how GSDME-dependent non-canonical pyroptosis induces vascular senescence and promotes aortic aneurysm development. Cleavage and activation of GSDME trigger non-canonical pyroptosis in the vascular wall, releasing inflammatory and pro-senescent factors that drive AAA progression. GSDME deletion suppresses vascular senescence and limits arterial dilation, whereas its restoration in vascular smooth muscle cells (VSMCs) reinstates senescence and exacerbates pathology. In contrast, senolytic therapy mitigates AAA in mice with VSMC-specific GSDME rescue. Thus, GSDME-mediated pyroptosis accelerates AAA development by inducing and amplifying VSMC senescence within the vascular microenvironment.

tagged on the 5′ end (that is, the 3′ end of an mRNA transcript) with a unique molecular identifier (UMI) and cell barcode indicating its cell of origin. Whole-transcriptome libraries were prepared using the BD Rhapsody single-cell whole-transcriptome amplification (WTA) workflow, including random priming and extension (RPE), RPE amplification PCR, and WTA index PCR. The libraries were quantified using a high-sensitivity DNA chip (Agilent) on a Bioanalyzer 2200 and the Qubit high-sensitivity DNA assay (Thermo Fisher Scientific). Sequencing was performed on an Illumina sequencer (Illumina) on a 150 bp paired-end run.

scRNA sequencing data analysis

Raw sequencing data were demultiplexed with CellRanger (v7.0.1), and UMI count matrices were generated using Seurat (v5.0.1). Doublets were removed with doubletFinder (v2.0.4), and cells with >10% mitochondrial gene content were excluded, yielding 14,393 cells for downstream analysis. The top 2000 highly variable genes were identified, and samples were integrated with Harmony (v1.2.0). Clustering (resolution 0.8) identified 20 clusters, visualized by UMAP. Marker genes were calculated using FindAllMarkers, and clusters were annotated with SingleR (v2.0.0). Differentially expressed genes were subjected to GO and KEGG enrichment, and pathway activities were quantified by GSVA (v1.46.0). CellChat (v1.6.1) was used to infer ligand–receptor interactions, focusing on SMC–immune cell crosstalk. Pseudotime trajectories of VSMCs and myeloid subsets were reconstructed with Monocle3 (v1.3.4). The raw data of scRNA-seq of our study is available in the Gene Expression Omnibus database (http://www.ncbi.nlm.nih.gov/geo) under accession codes GSE264071. The public scRNA-seq dataset obtained from the NCBI Gene Expression Omnibus (GEO) database under the accession number GSE239620 was processed and analyzed.

Statistical analysis

All results were presented as mean ± SEM. The distribution of data within all individual groups was verified by the Shapiro-Wilk test of normality. The statistical analysis was performed by Student's *t*-test (two groups) or analysis of variance (ANOVA) followed by Tukey-hoc test (more than two groups). Sample sizes were based on standard protocols in the field. The number of animals/samples in each group is indicated in the figure legend. Unless otherwise stated, the statistical significance level was set at 0.05. All statistical analyses were performed using GraphPad Prism 8.

Reporting summary

Further information on research design is available in the Nature Portfolio Reporting Summary linked to this article.

Data availability

The raw data of RNA-seq generated in this study of aortic tissue from WT and GSDME-KO mice have been deposited in the NCBI Sequence Read Archive (SRA) database under accession code PRJNA1094635. The raw data of scRNA-seq generated in this study is available in the Gene Expression Omnibus database under accession code GSE264071. The public RNA-seq dataset used in this study is available in the NCBI Gene Expression Omnibus (GEO) database under the accession code GSE47472. The public scRNA-seq dataset used in this study is available in the NCBI Gene Expression Omnibus (GEO) database under the accession code GSE239620. Source data are provided with this paper. All other data supporting the findings of this study are available from the corresponding author upon request. Source data are provided with this paper.

References

1. Evangelou, K. et al. Cellular senescence and cardiovascular diseases: moving to the "heart" of the problem. *Physiol. Rev.* **103**, 609–647 (2023).
2. Chi, C. et al. Exerkine fibronectin type-III domain-containing protein 5/irisin-enriched extracellular vesicles delay vascular ageing by increasing SIRT6 stability. *Eur. Heart J.* **43**, 4579–4595 (2022).
3. Grootaert, M. O. J., Finigan, A., Figg, N. L., Uryga, A. K. & Bennett, M. R. SIRT6 protects smooth muscle cells from senescence and reduces atherosclerosis. *Circ. Res.* **128**, 474–491 (2021).
4. Herman, A. B. et al. DPP4 inhibition impairs senohemostasis to improve plaque stability in atherosclerotic mice. J. Clin. Invest. 133, e165933 (2023).
5. Zychlinsky, A., Prevost, M. C. & Sansonetti, P. J. Shigella flexneri induces apoptosis in infected macrophages. *Nature* **358**, 167–169 (1992).
6. Strowig, T., Henao-Mejia, J., Elinav, E. & Flavell, R. Inflammasomes in health and disease. *Nature* **481**, 278–286 (2012).
7. Shi, J. et al. Cleavage of GSDMD by inflammatory caspases determines pyroptotic cell death. *Nature* **526**, 660–665 (2015).
8. Liu, X. et al. Inflammasome-activated gasdermin D causes pyroptosis by forming membrane pores. *Nature* **535**, 153–158 (2016).
9. Wang, Y. et al. Chemotherapy drugs induce pyroptosis through caspase-3 cleavage of a gasdermin. *Nature* **547**, 99–103 (2017).
10. Rogers, C. et al. Cleavage of DFNA5 by caspase-3 during apoptosis mediates progression to secondary necrotic/pyroptotic cell death. *Nat. Commun.* **8**, 14128 (2017).
11. Ouyang, S. X. et al. Gasdermin-E-dependent non-canonical pyroptosis promotes drug-induced liver failure by promoting CPS1 deISGylation and degradation. *Adv. Sci.* **11**, e2305715 (2024).
12. Zhu, J. H. et al. GSDME promotes MASLD by regulating pyroptosis, Drp1 citrullination-dependent mitochondrial dynamic, and energy balance in intestine and liver. *Cell Death Differ.* **31**, 1467–1486 (2024).
13. Wei, Y. et al. GSDME-mediated pyroptosis promotes the progression and associated inflammation of atherosclerosis. *Nat. Commun.* **14**, 929 (2023).
14. Wu, Y. et al. Caspase-4/11-mediated pulmonary artery endothelial cell pyroptosis contributes to pulmonary arterial hypertension. *Hypertension* **79**, 536–548 (2022).
15. Fu, H. et al. Activating alpha7nAChR ameliorates abdominal aortic aneurysm through inhibiting pyroptosis mediated by NLRP3 inflammasome. *Acta Pharmacol. Sin.* **43**, 2585–2595 (2022).
16. Zhao, Y. et al. Colchicine protects against the development of experimental abdominal aortic aneurysm. *Clin. Sci.* **137**, 1533–1545 (2023).
17. Gao, J. et al. Gasdermin D deficiency in vascular smooth muscle cells ameliorates abdominal aortic aneurysm through reducing putrescine synthesis. *Adv. Sci.* **10**, e2204038 (2023).
18. Ye, B. et al. Macrophage-derived GSDMD promotes abdominal aortic aneurysm and aortic smooth muscle cells pyroptosis. *Int. Immunopharmacol.* **128**, 111554 (2024).
19. Fang, Z. et al. Gasdermin D affects aortic vascular smooth muscle cell pyroptosis and Ang II-induced vascular remodeling. *Heliyon* **9**, e16619 (2023).
20. Sakalihasan, N. et al. Abdominal aortic aneurysms. *Nat. Rev. Dis. Prim.* **4**, 34 (2018).
21. Golledge, J., Thanigaimani, S., Powell, J. T. & Tsao, P. S. Pathogenesis and management of abdominal aortic aneurysm. *Eur. Heart J.* **44**, 2682–2697 (2023).
22. Senemaud, J. et al. Translational relevance and recent advances of animal models of abdominal aortic aneurysm. *Arterioscler. Thromb. Vasc. Biol.* **37**, 401–410 (2017).
23. Song, T. et al. SLC44A2 regulates vascular smooth muscle cell phenotypic switching and aortic aneurysm. J. Clin. Invest. 134, e173690 (2024).
24. Mu, X. et al. Androgen aggravates aortic aneurysms via suppression of PD-1 in mice. J. Clin. Invest. 134, e169085 (2024).
25. Dick, S. A. et al. Three tissue resident macrophage subsets coexist across organs with conserved origins and life cycles. *Sci. Immunol.* **7**, eabf7777 (2022).
26. Raffort, J. et al. Monocytes and macrophages in abdominal aortic aneurysm. *Nat. Rev. Cardiol.* **14**, 457–471 (2017).
27. Sun, D. Y. et al. Pro-ferroptotic signaling promotes arterial aging via vascular smooth muscle cell senescence. *Nat. Commun.* **15**, 1429 (2024).
28. Saul, D. et al. Osteochondroprogenitor cells and neutrophils expressing p21 and senescence markers modulate fracture repair. J. Clin. Invest. 134, e179834 (2024).
29. Lee, J. Y. et al. An in vivo screening platform identifies senolytic compounds that target p16INK4a+ fibroblasts in lung fibrosis. J. Clin. Invest. 134, e173371 (2024).
30. Chang, T. Y. et al. Combined HDAC8 and checkpoint kinase inhibition induces tumor-selective synthetic lethality in preclinical models. J. Clin. Invest. 134, e165448 (2024).
31. Sharma, N. et al. Deficiency of IL12p40 (interleukin 12 p40) promotes Ang II (Angiotensin II)-induced abdominal aortic aneurysm. *Arterioscler. Thromb. Vasc. Biol.* **39**, 212–223 (2019).
32. Acosta, J. C. et al. Chemokine signaling via the CXCR2 receptor reinforces senescence. *Cell* **133**, 1006–1018 (2008).

33. Coutu, D. L., Francois, M. & Galipeau, J. Inhibition of cellular senescence by developmentally regulated FGF receptors in mesenchymal stem cells. *Blood* **117**, 6801–6812 (2011).
34. Quintana, R. A. & Taylor, W. R. Cellular mechanisms of aortic aneurysm formation. *Circ. Res.* **124**, 607–618 (2019).
35. Schyns, J. et al. Non-classical tissue monocytes and two functionally distinct populations of interstitial macrophages populate the mouse lung. *Nat. Commun.* **10**, 3964 (2019).
36. Sun, S. J. et al. Gasdermin-E-mediated pyroptosis drives immune checkpoint inhibitor-associated myocarditis via cGAS-STING activation. *Nat. Commun.* **15**, 6640 (2024).
37. Ma, F. et al. Gasdermin E dictates inflammatory responses by controlling the mode of neutrophil death. *Nat. Commun.* **15**, 386 (2024).
38. Ai, Y. L. et al. Mannose antagonizes GSDME-mediated pyroptosis through AMPK activated by metabolite GlcNAc-6P. *Cell Res.* **33**, 904–922 (2023).
39. Wang, S. et al. Gasdermin C sensitizes tumor cells to PARP inhibitor therapy in cancer models. J. Clin. Invest. 134, e166841 (2024).
40. Fu, M. et al. Single-cell multiomic analysis identifies macrophage subpopulations in promoting cardiac repair. J. Clin. Invest. 134, e175297 (2024).
41. Mitchell, C. A. et al. Stromal niche inflammation mediated by IL-1 signalling is a targetable driver of haematopoietic ageing. *Nat. Cell Biol.* **25**, 30–41 (2023).
42. Gardner, S. E., Humphry, M., Bennett, M. R. & Clarke, M. C. Senescent vascular smooth muscle cells drive inflammation through an interleukin-1alpha-dependent senescence-associated secretory phenotype. *Arterioscler. Thromb. Vasc. Biol.* **35**, 1963–1974 (2015).
43. Li, L. et al. Inhibition of ACSS2-mediated histone crotonylation alleviates kidney fibrosis via IL-1beta-dependent macrophage activation and tubular cell senescence. *Nat. Commun.* **15**, 3200 (2024).
44. Xia, S. et al. Synthetic protein circuits for programmable control of mammalian cell death. Cell 187, 2785–2800.e16 (2024).
45. Galluzzi, L. et al. Molecular mechanisms of cell death: recommendations of the Nomenclature Committee on Cell Death 2018. *Cell Death Differ.* **25**, 486–541 (2018).
46. Lazarov, T., Juarez-Carreno, S., Cox, N. & Geissmann, F. Physiology and diseases of tissue-resident macrophages. *Nature* **618**, 698–707 (2023).
47. Al-Rifai, R. et al. JAK2V617F mutation drives vascular resident macrophages toward a pathogenic phenotype and promotes dissecting aortic aneurysm. *Nat. Commun.* **13**, 6592 (2022).
48. Xu, M. et al. Senolytics improve physical function and increase lifespan in old age. *Nat. Med.* **24**, 1246–1256 (2018).
49. Parvizi, M. et al. Senolytic agents lessen the severity of abdominal aortic aneurysm in aged mice. *Exp. Gerontol.* **151**, 111416 (2021).
50. Shen, M., Hu, M., Fedak, P. W. M., Oudit, G. Y. & Kassiri, Z. Cell-specific functions of ADAM17 regulate the progression of thoracic aortic aneurysm. *Circ. Res.* **123**, 372–388 (2018).
51. Zhao, G. et al. Single-cell RNA sequencing reveals the cellular heterogeneity of aneurysmal infrarenal abdominal aorta. *Cardiovasc. Res.* **117**, 1402–1416 (2021).
52. Luo, S. et al. Endothelial HDAC1-ZEB2-NuRD complex drives aortic aneurysm and dissection through regulation of protein S-sulfhydration. *Circulation* **147**, 1382–1403 (2023).
53. Novais, E. J. et al. Long-term treatment with senolytic drugs Dasatinib and Quercetin ameliorates age-dependent intervertebral disc degeneration in mice. *Nat. Commun.* **12**, 5213 (2021).
54. Fu, J. T. et al. Targeting EFHD2 inhibits interferon-gamma signaling and ameliorates non-alcoholic steatohepatitis. *J. Hepatol.* **81**, 389–403 (2024).
55. Peshkova, I. O. et al. IL-27 receptor-regulated stress myelopoiesis drives abdominal aortic aneurysm development. *Nat. Commun.* **10**, 5046 (2019).
56. Wu, X., Lu, M., Yun, D., Gao, S. & Sun, F. Long-read single-cell sequencing reveals the transcriptional landscape of spermatogenesis in obstructive azoospermia and sertoli cell-only patients. QJM 117, 422–435 (2024).
57. Lin, S. M. et al. Hyperactive mTORC1 in lung mesenchyme induces endothelial cell dysfunction and pulmonary vascular remodeling. J. Clin. Invest. 134, e172116 (2023).

Acknowledgements

This work was supported by the grants from the National Natural Science Foundation of China (82274030 [D.J.L.], 81971306 [D.J.L.], 82504936 [S.J.S.], and 82373927 [P.W.]), Shanghai Science and Technology Commission (LJ2024083 [P.W.], 24YF2733300 [S.J.S.], and 21XD1424900 [P.W.]), and Tongji University-Fundamental Research Funds for the Central Universities (22120210560 [D.J.L.]). We thank the patients and their families.

Author contributions

P.W., D.J.L., and J.Z. conceived and designed research; S.J.S., Z.Z., G.Y.Z., J.J.W., and Y.X.Z. performed experiments; J.Z. and J.J.W. provided patents samples; W.B.W, Y.Z., H.Y., Q.C., J.W.W., F.M.S., and J.B.Z. analyzed data. S.J.S., D.J.L., and P.W. wrote the manuscript. S.J.S., P.W., and D.J.L. provided funding. All authors contributed with productive discussions and knowledge to the final version of this manuscript.

Competing interests

The authors declared no competing interests.

Additional information

Supplementary information The online version contains supplementary material available at https://doi.org/10.1038/s41467-025-66103-1.

Correspondence and requests for materials should be addressed to Jian Zhou, Dong-Jie Li or Pei Wang.

Peer review information *Nature Communications* thanks Yue Wu, Baohui Xu, Jiayu Ye, and the other anonymous reviewer(s) for their contribution to the peer review of this work. A peer review file is available.